APPLIED SCIENCES AND ENGINEERING

Electrically compensated, tattoo-like electrodes for epidermal electrophysiology at scale

Youhua Wang[1,2], Lang Yin[1,2], Yunzhao Bai[1,2], Siyi Liu[3], Liu Wang[3,4], Ying Zhou[1,2], Chao Hou[1,2], Zhaoyu Yang[1,2], Hao Wu[1,2], Jiaji Ma[1,2], Yaoxin Shen[1,2], Pengfei Deng[1,2], Shuchang Zhang[1,2], Tangjian Duan[1,2], Zehan Li[1,2], Junhui Ren[1,2], Lin Xiao[1,2], Zhouping Yin[1,2], Nanshu Lu[3,5,6]*, YongAn Huang[1,2]*

Epidermal electrophysiology is widely carried out for disease diagnosis, performance monitoring, human-machine interaction, etc. Compared with thick, stiff, and irritating gel electrodes, emerging tattoo-like epidermal electrodes offer much better wearability and versatility. However, state-of-the-art tattoo-like electrodes are limited in size (e.g., centimeters) to perform electrophysiology at scale due to challenges including large-area fabrication, skin lamination, and electrical interference from long interconnects. Therefore, we report large-area, soft, breathable, substrate- and encapsulation-free electrodes designed into transformable filamentary serpentines that can be rapidly fabricated by cut-and-paste method. We propose a Cartan curve–inspired transfer process to minimize strain in the electrodes when laminated on nondevelopable skin surfaces. Unwanted signals picked up by the unencapsulated interconnects can be eliminated through a previously unexplored electrical compensation strategy. These tattoo-like electrodes can comfortably cover the whole chest, forearm, or neck for applications such as multichannel electrocardiography, sign language recognition, prosthetic control or mapping of neck activities.

INTRODUCTION

Electrophysiological activities, such as electrocardiogram (ECG), surface electromyogram (sEMG), and electroencephalogram (EEG), are ubiquitous on human skin surfaces. Electrical impulses generated by numerous pacemaker cells and neurons transmit through the complex three-dimensional (3D) volume of electrically conductive tissues and skin, eventually become spatiotemporally varying electrical potentials on skin surfaces, as illustrated in Fig. 1A. We conducted a multichannel measurement on the upper body shown in fig. S1A to demonstrate the complexity of large-area epidermal electrophysiology. Figure S1B plots four snapshots of the measured arm-chest-venter surface potential distributions, which come from both heart and muscle activities. When the left hand lifted a 2-kg discus and the right hand gripped a hand dynamometer with a force of 10 kg, the amplitude of the chest potential changed from −2.62 to 1.34 mV within only 0.06 s. Multichannel epidermal electrophysiology is widely used as a powerful diagnostic and research tool for monitoring and studying the brain, the heart, and different muscles (*1*). For example, 12-lead ECG is a standard clinical procedure for noninvasive diagnosis of arrhythmias and other heart diseases. Although Ag/AgCl gel electrodes are current gold standards for epidermal electrophysiology, the gel is known to be irritating to the skin and easy to dry out, which limit their long-term use. Moreover, using multiple gel electrodes for multichannel electrophysiology involves multiple lead wires and snap buttons (fig. S1A) (*2*), which substantially compromises the comfort, mobility, and signal quality under motion (*3*). As a result, many dry electrodes have been developed over the years including rigid boxes with metallic pads (e.g., Delsys Trigno Avanti wearable EMG system), metal films on plastics (*4*), carbon composites (*5*), and conductive fabrics (*6*). However, dry electrodes generally suffer from poor skin integration, low signal-to-noise ratio (*7*), and small area coverage (*8*).

With the advancement of novel soft materials (*9*–*11*) and mechanical designs (*12*–*14*), the emerging ultrathin and tissue-soft electronic skins (*15*, *16*) or epidermal electronics (*12*, *13*, *17*) have been demonstrated with substantially enhanced skin conformability and comfort. Nevertheless, there are three major challenges to scale them up for large-area electrophysiology. First, most existing epidermal electronics are in the size of a few centimeters, which is limited by their fabrication processes. Latest progress on large-area tattoo-like electrodes was full-scalp multichannel EEG electrodes fabricated on an 8-inch silicon wafer (*17*). However, microfabrication on large wafers is expensive and difficult for further scaling up. Second, without thick enough encapsulation layers, extended interconnects in direct contact with the skin, also named exposed epidermal interconnects (EEIs), can collect unwanted but substantial biopotentials that interfere with the signals collected by the measuring electrodes (*7*, *18*). Last, the geometrically nondevelopable nature of human skin surfaces can cause either prestretch or wrinkle in the ultrathin electrodes during skin lamination, which compromises the mechanical integrity or the conformability of the devices (*19*, *20*). Multiple solutions have been proposed to transfer ultrathin electronics to curvilinear surfaces. If the target surface is deformable, such as the case of digital eye camera, then the substrate is flattened before the circuits were transfer printed (*21*, *22*). Water-assisted transfer to nondevelopable surfaces has been widely used, but wrinkles and strains are inevitable (*23*). Conformal additive stamping method using an inflated balloon as the stamp has been invented as a very

[1]State Key Laboratory of Digital Manufacturing Equipment and Technology, Huazhong University of Science and Technology, Wuhan 430074, China. [2]Flexible Electronics Research Center, Huazhong University of Science and Technology, Wuhan 430074, China. [3]Center for Mechanics of Solids, Structures and Materials, Department of Aerospace Engineering and Engineering Mechanics, University of Texas at Austin, Austin, TX 78712, USA. [4]Department of Mechanical Engineering, Massachusetts Institute of Technology, Cambridge, MA 02139, USA. [5]Department of Biomedical Engineering, University of Texas at Austin, Austin, TX 78712, USA. [6]Texas Materials Institute, University of Texas at Austin, Austin, TX 78712, USA.
*Corresponding author. Email: yahuang@hust.edu.cn (Y.H.); nanshulu@utexas.edu (N.L.)

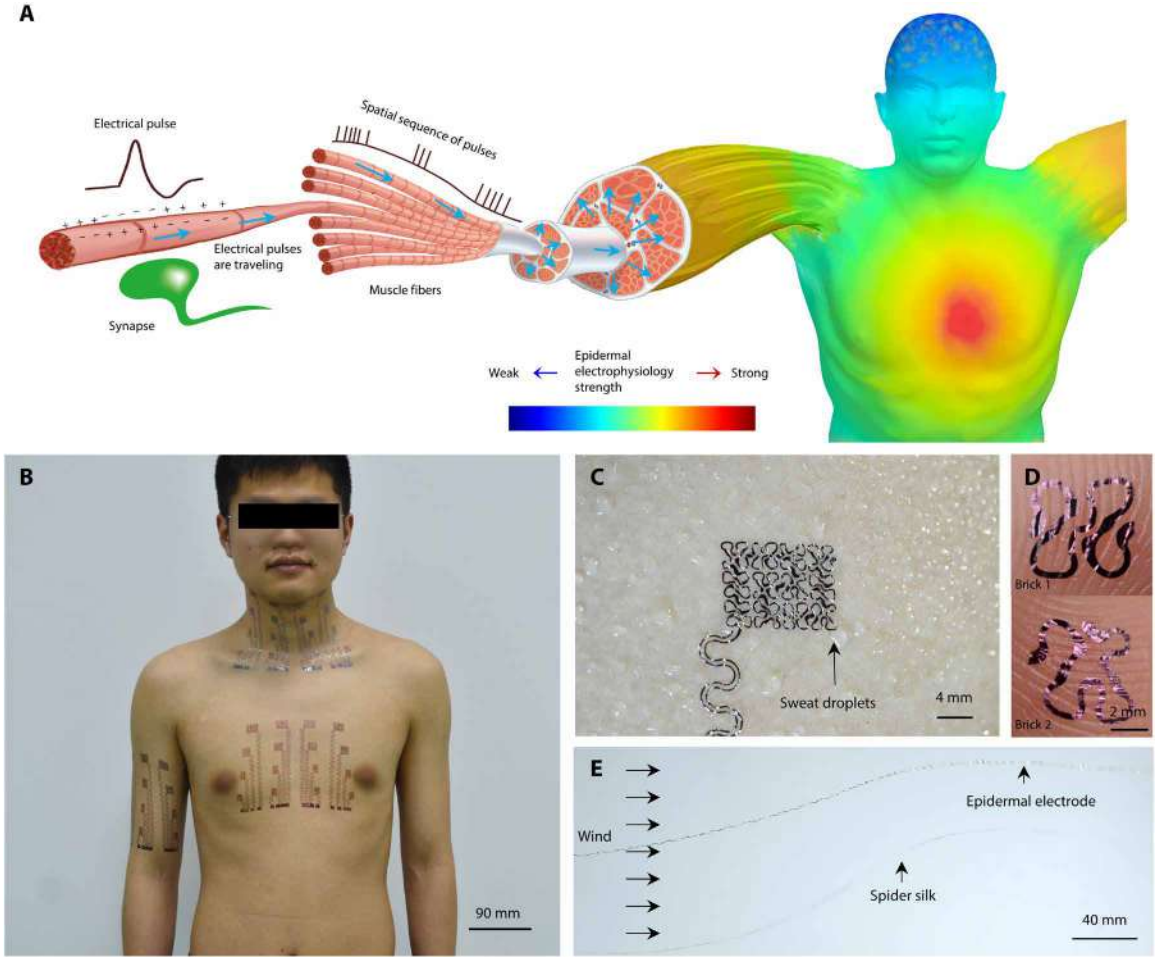

Fig. 1. Illustration of epidermal electrophysiology at scale. (**A**) Schematics of spatially varying electrophysiology over skin surface originating from internal muscle and organ activities. (**B**) Photograph of the body-scale epidermal electrodes. Photo credit: Youhua Wang, State Key Laboratory of Digital Manufacturing Equipment and Technology, Huazhong University of Science and Technology and Flexible Electronics Research Center, Huazhong University of Science and Technology. (**C**) Open-mesh filamentary serpentine network is unobstructive to sweating and sweat evaporation. Photo credit: Chao Hou, State Key Laboratory of Digital Manufacturing Equipment and Technology, Huazhong University of Science and Technology and Flexible Electronics Research Center, Huazhong University of Science and Technology. (**D**) Optical micrographs of two filamentary serpentine ribbons conforming to fingerprint topologies. Photo credit: Lin Xiao, State Key Laboratory of Digital Manufacturing Equipment and Technology, Huazhong University of Science and Technology and Flexible Electronics Research Center, Huazhong University of Science and Technology. (**E**) A filamentary serpentine ribbon flutters in wind similar to a single strand of spider silk. Photo credit: Chao Hou, State Key Laboratory of Digital Manufacturing Equipment and Technology, Huazhong University of Science and Technology and Flexible Electronics Research Center, Huazhong University of Science and Technology.

versatile transfer printing approach (*24*). However, during the printing step, the soft balloon surface has to stretch to fully conform to a 3D curvilinear target surface, which could induce nontrivial strains (>1%) in the devices as revealed in the paper. Therefore, none of the existing transfer printing methods is satisfactory to us. There are additional concerns associated with large-area tattoo-like epidermal electrodes such as how to maximize skin breathability including sweat evaporation and heat dissipation. Existing solutions include using a porous or perforated substrate (*17*, *25*) or substrate-free open-mesh devices thin enough to attach by van der Waals forces (*3*, *26*). In summary, the creation of large-area, substrate-free epidermal electrodes demands new fabrication, skin lamination, and noise reduction strategies that are compatible with the scale of the measurement.

This paper offers a comprehensive solution to large-area, breathable, mechanically robust, and high-fidelity epidermal electrodes through the combination of a scalable manufacturing process, strain-limiting transfer-printing process, and a signal compensation theory to cancel signals picked up by the EEIs. We have easily scaled up our previous cut-and-paste process of manufacturing substrate-free, micrometer-thick, and stretchable epidermal electrodes (*3*) to achieve large-area, multichannel electrophysiology. Figure 1B shows the possible coverage of our large-area epidermal electrodes over different body parts. These electrodes are substrate-free filamentary serpentine ribbons as thin as 1.2 μm, rendering the device sweat and heat permeable (Fig. 1C), skin conformable (Fig. 1D), and extremely stretchable and lightweight similar to a spider silk fiber (Fig. 1E). A mathematical concept, Cartan development, is used to guide the transfer of substrate-free, filamentary serpentines to 3D curvilinear skin surfaces without distortion or wrinkling. A signal compensation theory and the corresponding circuit design are developed to eliminate the electrical interference of the long EEIs. The benefits of

this new class of epidermal electrodes will be quantified in terms of mitigating mechanical strain, dissipating heat and sweat, and stabilizing signals. Our epidermal electrodes have been successfully applied to capture various biopotentials in high fidelity at scale, including 16-channel sEMG on the forearm for the interpretation of sign language and prosthesis control, 16-channel sEMG on the neck for activity classification (e.g., swallowing, chewing, and turning), and 16-channel ECG on the chest for cardiac health monitoring.

RESULTS

Signal compensation theory and experimental validation

The photolithographic fabrication of epidermal electronics is difficult to scale up due to the size limitation of wafers, masks, and microfabrication tools such as spin coaters, vacuum deposition chambers, and mask aligners. Alternatively, the cut-and-paste fabrication process we developed before only involves a mechanical cutter plotter for patterning, as well as a flexible mat as the temporary cutting support (*27*). As a result, it features many advantages such as mask- and wafer-free dry process, low cost, and scalability. The experimental details of fabricating large-area tattoo-like electrodes using the cut-and-paste method are offered in Materials and Methods. However, the cut-and-paste method is incapable of selective encapsulation. It is not a big limiting factor when we fabricated small-sized epidermal electronics (*3*, *27*). However, when the interconnects have larger area coverage than the electrodes, which is the case of the multichannel epidermal electrodes, the EEI in direct contact with the skin could pick up noises that are large enough to interfere with the desirable signals. The cut-and-paste method would only be applicable to epidermal electrophysiology at scale after overcoming this challenge.

We therefore propose a signal compensation strategy to cope with unencapsulated EEIs. In this setup, the epidermal sensor is functionally divided into two parts: the acquisition module and the compensation module, as shown in fig. S2A. The 16-channel acquisition module is designed to cover a large area (126 mm by 166 mm; fig. S2B) for multichannel electrophysiology. Each channel of the acquisition module encompasses an epidermal working electrode (EWE), an EEI, and an epidermal compensation branch (ECB) parallel to each EEI (fig. S2C). The compensation module is much more compact (68 mm by 42 mm; fig. S2B), aiming to eliminate the unwanted signals collected by the EEIs in the acquisition module. All EWEs in the acquisition module and epidermal compensation electrodes (ECEs) in the compensation module are Peano-based fractal geometries (*13*) constructed using two basic elements called bricks (Fig. 1D and fig. S2, C and D). Both types of bricks are stackable in horizontal or vertical directions. Bricks 1 and 2 are for extending and making a right/left turn, respectively. Except the interconnect direction, both bricks have the same features: the size of 4 mm by 4 mm, high areal coverage (the area of filament divided by the overall area of a brick) of 44.7%, excellent conformability (fig. S3, A and B), enormous stretchability while freestanding (240% for brick 1 and 560% for brick 2 as shown in fig. S3C), and high stretchability (18%) when laminated on the skin (fig. S3, E to H), which is compatible with known skin deformability (*17*). Considering that during fabrication, removing the extraneous parts occasionally causes an ultrathin filamentary electrode to intertwine with itself during the cut-and-paste process, the mechanical robustness of the two bricks also enables easy recovery of the electrode's original shape during fabrication (fig. S3D and movie S1).

The compensation theory we want to propose is described in Fig. 2. Instead of the conventional lumped-parameter equivalent circuit model (*7*, *18*), we built a distributed-parameter equivalent circuit model across the skin-conductor interface as illustrated by the top left inset in Fig. 2A. The distributed model accounts for the area of the electrodes and the interconnects as well as the skin and muscle covered by them. Assuming full conformability as confirmed in Fig. 1D, the impedance to electrophysiology is a summation of the impedance of the electrical double layer formed at the conductor-skin interface and the impedance of the skin and the muscle. As the impedance of the stratum corneum is several orders of magnitudes higher than that of the dermis and the muscle (*28*, *29*), it is reasonable to regard the electrical potential in the dermis and muscle layer as the voltage sources and assume that the metal conductors on the skin do not affect the distribution of the electrical potential in the dermis and the muscles. The thickness of the stratum corneum is as thin as tens of micrometers; hence, the transverse current flow in stratum corneum can be neglected. According to the Kirchhoff's current law, the measurable voltage in the conductor is

$$V = \frac{\Sigma_{i=1}^{n} \frac{E_i}{Z_i}}{\Sigma_{i=1}^{n} \frac{1}{Z_i}} \tag{1}$$

where E_i is the electrical potential of voltage source i and Z_i is the impedance at location i.

Equation 1 can be divided into two parts

$$V = \left(\frac{\Sigma_{i=1}^{m} \frac{E_i}{Z_i}}{\Sigma_{i=1}^{m} \frac{1}{Z_i}}\right)_{\text{EWE}} \frac{\Sigma_{i=1}^{m} \frac{1}{Z_i}}{\Sigma_{i=1}^{n} \frac{1}{Z_i}} + \left(\frac{\Sigma_{i=m+1}^{n} \frac{E_i}{Z_i}}{\Sigma_{i=m+1}^{n} \frac{1}{Z_i}}\right)_{\text{EEI}} \frac{\Sigma_{i=m+1}^{n} \frac{1}{Z_i}}{\Sigma_{i=1}^{n} \frac{1}{Z_i}} \tag{2}$$

The first part and the second part represent the signals recorded by the EWE and the EEI, respectively. It is clear that V is the weighted average of E_i and, hence, two important corollaries can arise. First, the E_i values from the EEIs interfere with those from the EWEs. Second, to precisely acquire the potential of one point, shrinking the area of the EWE is necessary because the measured V reflects the average of the E_i over this area. A continuous form of this model is offered in the Supplementary Materials.

To eliminate the signals picked up by the EEIs, we design an ECB of the same length as the EEI to be closely parallel to the EEI (fig. S2C). However, this method, named partial compensation, cannot completely eliminate the noise, as discussed in the Supplementary Materials. Therefore, an ECE is further introduced to connect to the ECB, as shown in Fig. 2A. The channel order of ECEs in fig. S2D corresponds to that of the EWEs in fig. S2B. The impedance of the ECE is designed to be

$$Z = \frac{1}{\int_{L_1}^{L_1+L_2} \frac{1}{z} dl} \tag{3}$$

where L_1 and L_2 are the lengths of the filamentary serpentine ribbons of the EEI and the EWE, respectively, and z represents the unit area impedance to electrophysiology, which is a lump sum of the impedance of the metal-skin electrical double layer and the impedance of the stratum corneum. A detailed discussion of z is included in the Supplementary Materials. z could vary with body locations and from person to person. To ensure uniform electrical property

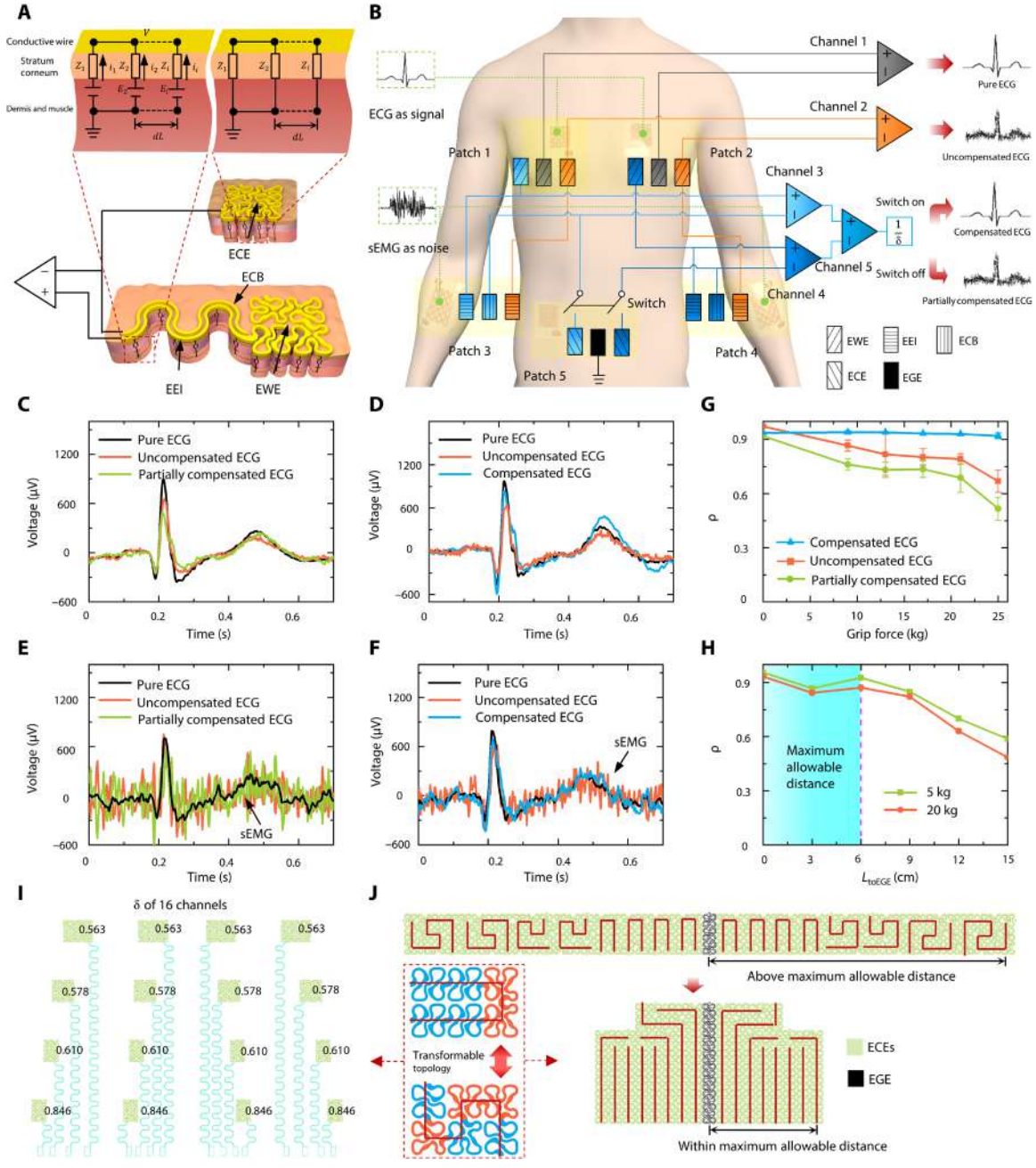

Fig. 2. Signal compensation model and experimental validation. (**A**) Schematic of EWEs, exposed EEIs, ECBs, ECEs, and their equivalent circuits for electrode-skin interface. (**B**) Circuit design of the validation experiment with colors denoting channel connection and shades representing the functionality of electrodes. (**C**) ECG measured with switch off and forearm relaxed. (**D**) ECG measured with switch on and forearm relaxed. (**E**) ECG measured with switch off and forearm gripping. (**F**) ECG measured with switch on and forearm gripping. (**G**) Pearson correlation coefficient (PCC) with respect to grip force. (**H**) PCC with respect to the distance L_{toEGE} between the epidermal ground electrode (EGE) and the ECEs. (**I**) Length fraction δ of 16 channels. (**J**) The transforming process of the ECE. The dash rectangle represents the topology transformability of the electrodes using two stackable bricks.

of the skin (fig. S4A), we applied conductive gel less than 5 μm thick on the skin before transferring the epidermal electrodes. It has to be pointed out that applying too much conductive gel on the skin may reduce the impedance of the stratum corneum so much that the key assumption of the compensation theory is violated. We designed the filamentary length of the ECE to be identical to that of the EWE and assumed that they have similar z due to the gel application. The only distinction between ECEs and EWEs is that the former is required to be laminated at a location where the electrical potential in dermis layers and muscles can be regarded as zero, also known as the ground (top right inset in Fig. 2A).

Taking $\delta = \frac{L_2}{L_1 + L_2}$ to be the length fraction of the EWE, the actually measured signal is related to the signal picked up by the EWE through

$$V = V_{\mathrm{EWE}} \cdot \delta + V_{\mathrm{othernoise}} \quad (4)$$

It is therefore apparent that the dimensionless parameter δ must be cautiously selected such that the other background noises (e.g., thermal noises) are not going to overwhelm the desirable signal. Background noises will be investigated later.

To validate this signal compensation theory, we carried out a carefully designed experiment, as illustrated in Fig. 2B and fig. S4B. Our primary objective was to quantify and then eliminate the impact of sEMG on ECG using this strategy. ECG, owing to its recognizable features, such as the P, Q, R, S, and T waves, was collected by EWEs as the target signal; while sEMG, which has higher frequency and smaller amplitude, was collected by EEIs as noise added to the ECG.

The colored rectangles in Fig. 2B correspond to the same colored but magnified filamentary serpentine blocks in fig. S4B. Different rectangle colors represent different channel connections, and different shades represent different types of electrodes. Patches 1 and 2, each containing three EWEs, were attached on the two opposite sides of the chest with a distance of 10 cm to collect ECG. Patches 3 and 4, each containing two sEMG electrodes to mimic EEIs and one ECB, were attached on two forearms to collect sEMG. Patch 5, including two ECEs and one epidermal ground electrode (EGE), was attached on the lower right abdomen, where the biopotential is commonly regarded to be stable. In each patch, the conductive parts consisted of a cluster of closely parallel filamentary serpentines of equal length and equal width, as shown in the blown-up view in fig. S4B. More detailed geometrical designs of these patches are discussed in Materials and Methods.

The connection of the electrodes is a bit complicated so it is described in detail as follows. The two gray-colored EWEs in patches 1 and 2 were connected to channel 1 to collect pure ECG. The two orange-colored sEMG electrodes in patches 3 and 4 were connected to channel 2 through the two orange-colored EWEs in patches 1 and 2, respectively, to collect uncompensated ECG with sEMG superimposed on the ECG. The positive port of channel 3 (light blue) was connected to the blue-colored EWEs in patch 1 (right chest) and the sEMG electrode (referred as the EEI) in patch 3 (right arm). The negative port of channel 3 was connected to the ECB in patch 3 and to the right ECE in patch 5 through a switch. Similar connections were implemented for dark blue–colored channel 4 over the left part of the body. The output signals from channels 3 and 4 were put through a second differential channel, channel 5. The output from channel 5 divided by δ was considered to be compensated ECG when the switches were on and partially compensated ECG when the switches were off. More details of this compensation theory and circuit design are provided in the Supplementary Materials.

The output signals from channels 1, 2, and 5 are plotted in Fig. 2 (C to F). The black, orange, green, and blue curves represent pure, uncompensated, partially compensated, and compensated ECG, respectively. When the forearm was fully relaxed, there was no sEMG on the forearm; hence, all three channels of ECG signals appeared to be very similar, whether the switch in patch 5 is off (partially compensated; Fig. 2C) or on (compensated; Fig. 2D). However, when the participant intentionally tensed the forearm muscles by gripping, sEMG showed up as noise superimposed on ECG in both uncompensated and partially compensated ECG (Fig. 2E). In contrast, the compensated ECG remained as clean as the pure ECG despite the sEMG contamination (Fig. 2F and movie S2), which successfully validated our compensation strategy.

To further quantify the effectiveness of the compensation, we use Pearson correlation coefficient (PCC) to quantify the similarity of the measured signal to the pure ECG. The definition of PCC is included in the Supplementary Materials. Stronger sEMG contamination is expected to reduce the PCC. The participant was asked to grip a hand dynamometer with different strengths as a way to tune the amplitude of sEMG. Figure 2G shows that as the grip force increased, the PCC of compensated ECG (blue curve with triangular markers) stayed larger than 0.92 (its average is 0.93), whereas the PCCs of uncompensated ECG (red curve with square markers) and partially compensated ECG (green curve with round dots) decreased remarkably. These findings further validated that the compensation circuit is able to eliminate both weak and strong noises. Furthermore, ECEs should be placed at zero-potential area, i.e., near the EGE. The ECEs should not be directly connected to EGE, as the ECE impedance should match with that of the EWE as mentioned before. The theoretical analysis in the Supplementary Materials indicates that the potential gradient near the EGE and the distance L_{toEGE} between the ECEs and the EGE are two key factors affecting the compensation precision. We therefore also used PCC to study the effect of the distance between the ECEs and the EGE. The curves in Fig. 2H show that if L_{toEGE} was beyond 6 cm, then the PCC of the compensated ECG declined substantially for both moderate (5 kg; green) and heavy grip forces (20 kg; red). Therefore, 6 cm is regarded as the maximum allowable distance for the compensation theory to be valid. It is noted that the maximum allowable distance of sEMG on static muscles can be taken as 6 cm because ECG is much stronger than sEMG and, therefore, its spatial gradient is also larger on static muscles.

With the above theoretical and experimental setups, we should revisit the electrode design to complete the picture. There are two competing electrical considerations that set the size of the EWE. On the one hand, smaller size of EWEs means higher spatial resolution for electrophysiology. On the other hand, the discounting effect of the δ given by Eq. 4 demands a larger size of the EWE in comparison with the EEI. The balance between the two aspects helps set the optimal size of the EWE. Once the EWE size is set, the ECE design has the following two requirements: (i) An ECE has to have strictly the same electrode areal coverage as the corresponding EWE, (ii) L_{toEGE} of all ECEs should be less than 6 cm. A mechanical consideration is that the stretchability of all electrodes is expected to match that of human skin. Fractal-inspired structures are able to balance the trade-off between the area coverage and stretchability (*13*, *14*). Hence, we use fractal-inspired arrangements along with space-filling curves, such as Peano curves, to design our electrodes, as shown in Fig. 2 (I and J). The main reason we did not use conventional horseshoe-shaped serpentines as the filling curve is their low area filling ratio. For example, when the ratio of ribbon width to arc radius is 0.2, the maximum area filling ratio is only 24.05% for horseshoe-shaped serpentines (see the Supplementary Materials for details). The second reason is that the stacking of unit cells in different directions requires different transition blocks, which is detrimental for the generic design of the electrodes of many channels. Our electrode design has two interesting features: (i) nonuniform ribbon width to enhance the area filling ratio (as high as 44.7%) and (ii) two standard unit cells with the same area filling ration but different stacking orientations—an extension brick (brick 1) and a turning brick (brick 2) (Fig. 1D). The transformable topology of electrodes illustrated in the dashed box in Fig. 2J further provides two main benefits for device design. The dimensionless factor δ can be easily tuned

by changing the numbers of bricks according to the length of the EEI. The dimensionless factor δ of each channel is labeled in Fig. 2I. Furthermore, instead of simply duplicating the EWE (Fig. 2J, top), the topology of the ECE is transformed to be closer to the EGE using the same total number but a different combination of bricks 1 and 2 (Fig. 2J, bottom). For example, the EWE in channel 1 is constituted by 5 brick 1 and 7 brick 2 (fig. S2B), and the corresponding ECE includes 10 brick 1 and 2 brick 2 (fig. S2D). As a result, the maximum L_{toEGE} of ECEs reduces from 8.8 to 3.2 cm, below the maximum allowable distance of 6 cm. Different combinations of bricks 1 and 2 also affect the stretchability of an electrode. We studied this effect through finite element modeling (FEM) of an electrode composed of a total of nine bricks well attached on the skin. We varied the number of brick 2 in this electrode from four to six and stretched the skin by 18% in horizontal or vertical directions. The FEM results in fig. S5 (A to C) unveil that the maximum strain in the electrode material does not decrease monotonically with increasing number of brick 2. There seems to exist an optimal configuration, five units of brick 2 in this case. This is an interesting finding that deserves more in depth investigation in the future.

To study the noise caused by L_{toEGE} in the compacted compensation module itself, we measured the noise between the EGE and channel (CH) 8, the farthest ECE in the compensation module as shown in fig. S2D. We selected three body parts to carry out the measurements: the upper arm, the upper right back, and the lower right abdomen. The upper arm and the upper right back are locations where the compensation module stays when measuring sEMG of the forearm and the neck, respectively, while the lower right abdomen is where the compensation module is placed when measuring ECG on the chest. It is clear in fig. S6 that the noise on both the upper arm (~2 μV) and the upper right back (~3 μV) are much smaller than that on the lower right abdomen. The tiny noise collected by the compensation module at the upper arm and the upper right back can be negligible for the measurements of sEMG (at least 15 μV empirically). Although the noise on the lower right abdomen is ~8 μV, it can still be negligible compared with the magnitude of the measured ECG (at least 100 μV as shown in fig. S13B). It has to be pointed out that the maximum allowable distance may need to be adjusted if the compensation module is placed on the chest, as the current maximum allowable distance is determined for the lower right abdomen (fig. S4B).

Cartan development and Cartan transfer printing

The compensation strategy overcomes the electrical challenge unique to large-area tattoo-like electronics—noises picked up by long EEIs. In this section, we will deal with the mechanical challenge—how to achieve high-yield transfer of large-area tattoo-like electrodes to 3D curvilinear skin surfaces. It is not a big problem for small-area epidermal electronics as the skin can be locally approximated to be planar or cylindrical. However, the complex Gaussian curvature distributions of the whole chest (fig. S7A) and the whole forearm (fig. S7B) indicate that these surfaces can no longer be treated as developable surfaces, i.e., smooth surfaces with zero Gaussian curvature. As a result, the electrodes will be subjected to complex strain fields, which may yield fracture or wrinkle after direct transfer printing (DTP). To overcome this challenge, we propose a new transfer procedure inspired by the Cartan curves as illustrated in Fig. 3A. The pure rolling motion of a cylinder has an important feature that the rotation path $\boldsymbol{S}(t)$ at one point on the rim at instant t is equal to the path $\boldsymbol{s}(t)$ of the center of the cylinder. As shown in the top left panel in Fig. 3A, if $\boldsymbol{s}(t)$ is regarded as the device to be transferred on the cylinder, then this feature suggests that the device is not deformed in length after transferred to the substrate. We extended this concept into 3D space where a sphere rolls along a planar path $\boldsymbol{r}(t)$ at instant t and the curve connecting the contact points on the sphere is accordingly $\boldsymbol{R}(t)$, as illustrated by the bottom panel of Fig. 3A. The 3D curve $\boldsymbol{R}(t)$ can be regarded as the planar curve $\boldsymbol{r}(t)$ transfer printed on the spherical surface via pure rolling. As proved in the Supplementary Materials, the curve before and after transfer printing has the following features

$$|d\boldsymbol{s}| = |d\boldsymbol{S}| \tag{5}$$

$$\kappa_g = \kappa_G \tag{6}$$

where $|d\boldsymbol{s}|$ and $|d\boldsymbol{S}|$ are the lengths of infinitesimal arcs of $\boldsymbol{r}(t)$ and $\boldsymbol{R}(t)$, respectively. κ_g is the curvature of $\boldsymbol{r}(t)$, while κ_G is the geodesic curvature of $\boldsymbol{R}(t)$, as labeled in the top right panel of Fig. 3A. The curve $\boldsymbol{r}(t)$ is the Cartan development of $\boldsymbol{R}(t)$ (*30*, *31*). Both the rolling surface and the fixed surface can be further extended to be arbitrary continuous surfaces, which is proved in the Supplementary Materials.

We therefore designed the long serpentine filaments to be Cartan curves that can be transferred to nondevelopable surfaces by Cartan transfer printing (CTP). Our filaments have a thickness of 1.2 μm, a width of 300 μm, and lengths in the order of centimeters. For modeling purpose, the long filaments are assumed to be Euler-Bernoulli beams due to their small width-to-length (<0.03) and thickness-to-width (0.004) ratios. The physical meanings of Eqs. 5 and 6 are that there is no tension or compression along the centroid curve of the beam and there is no in-plane bending, respectively. The maximum principal strain due to the normal bending is given by $\varepsilon_{max} = h/(2R)$, or $\varepsilon_{max} = h\kappa_N/2$, where h is the thickness of the beam, R is the radius of the sphere, and κ_N is the normal curvature of arbitrary continuous surfaces. It is evident that negligible bending can be argued in the thickness direction due to their low thickness-to-radius ratio. Furthermore, ε_{max} is constant independent of the κ_g of $\boldsymbol{r}(t)$.

We carried out analytical and numerical modeling to compare strain induced in CTP versus DTP, a common method described by the inset of Fig. 3B. Figure 3B plots the maximum principal strains of arc-shaped ribbons with different radii transfer printed to different sized spheres using CTP or DTP obtained by FEM or analytical methods (see the Supplementary Materials). Both FEM and analytical results indicate that the maximum principal strain in the ribbon transferred by CTP is up to four orders of magnitudes lower than the ones transferred by DTP. The strain contours offered in Fig. 3C for a spiral and a serpentine ribbon transfer printed on a sphere via CTP also confirm the close-to-zero strain everywhere in the ribbon. Both ribbon structures are widely adopted for 3D antenna (*32*) and interconnects (*12*) in stretchable/flexible electronics. Movie S3 demonstrates the process of a curved filament transferring to a hemisphere by CTP.

To transfer complicated 2D patterns, in principle, we suppose the target surface to be fixed, and the donor substrate is rolling gradually along the pattern, similar to the processes of transferring a curved filament in Fig. 3A, while slightly deformed to achieve locally conformal contact with the target surface, as illustrated in Fig. 3D. The difference between transferring curved filaments and complicate

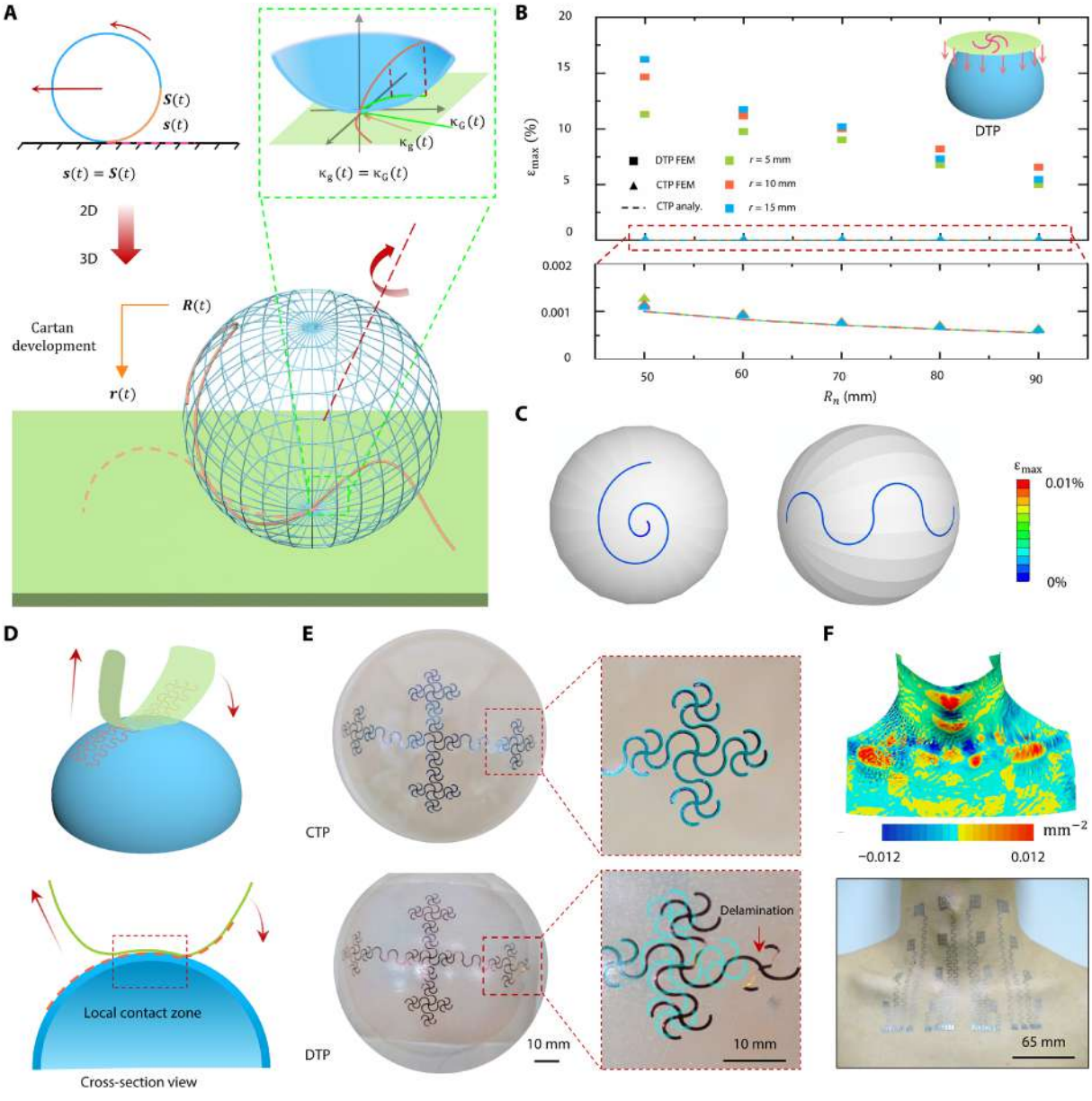

Fig. 3. Cartan transfer printing of large-area epidermal electrodes. (**A**) Schematic of Cartan transfer printing (CTP). (**B**) Maximum principal strain of circular arcs of different radii transferred on spherical surfaces of different radii by DTP and CTP. (**C**) FEM results of curves, such as a spiral and a serpentine, transferred on spherical surfaces. (**D**) CTP of complex patterns. (**E**) Optical images of patterns transfer printed by CTP (top) and DTP (bottom). The cyan is the untransferred pattern. (**F**) Gaussian curvature map of neck (top) and large-area tattoo-like electrodes laminated on neck through CTP (bottom). Photo credit: Youhua Wang, State Key Laboratory of Digital Manufacturing Equipment and Technology, Huazhong University of Science and Technology; Flexible Electronics Research Center, Huazhong University of Science and Technology.

patterns is that the contacting paths are ribbons with a small but finite width for the latter. The conformal width relies on the geometrical properties of the target surface and the mechanical properties of the donor substrate (*33*). Larger conformal width is possible if the Gaussian curvature of the target surface is small or the donor substrate is stretchable. However, bendable but not stretchable donor substrates (an inextensible cloth in this paper) are preferred according to the CTP mathematics. Figure S8 and movie S4 offer detailed instructions for transferring a 2D cross pattern from a bendable donor substrate to a hemispherical target surface. The cross pattern can be divided into four branches and, thus, was transferred after adjusting the donor substrate four times. The wet cloth (received devices from water transfer paper that supported the device during cutting) covered by branch 1 was first well laminated on the hemisphere coated with liquid adhesive (step I). The cloth was dried by napkins to detach from the hemisphere, leaving branch 1 printed on the hemisphere (step II). During steps I and II, other ribbons were carefully avoided to touch the hemispheric surface. Branches 2 to 4 (steps III to VI) could be transferred sequentially through bending and rolling of the donor substrate similar to steps I and II.

Last, the whole pattern was completely transferred onto the target surface (step VI). The optical images of Fig. 3E display the cross pattern transfer printed by CTP (top) and DTP (bottom). By overlapping the transferred (dark) and untransferred (cyan) patterns, it is visible that the pattern was fully preserved by CTP, whereas the pattern transferred by DTP was distorted and even delaminated. The complexity of human skin surface can be well illustrated by a surface Gaussian curvature map as shown in the top panel of Fig. 3F. Nevertheless, the large-area tattoo-like electrodes can be transfer printed to the skin with no distortion or detachment, as evident in the bottom panel of Fig. 3F. Despite the CTP process induces negligible strains to the pattern, the yield of CTP depends on the topology of the target surfaces. For almost developable surfaces, such as arms and male chests, the yield is high. A skilled person can succeed almost 100%. However, for nondevelopable surfaces such as the neck region, a skilled person not familiar with this region can transfer successfully after three to four trials. We have to admit that manually adjusting the donor substrate is not always perfectly controlled and could be quite time consuming. The substrate-free electrodes could be damaged when rubbed against clothes. A possible remedy as used by previous researchers (*34*, *35*) is to spray commercial liquid bandage over the electrodes, which could form a micrometer-thick transparent protective layer after drying.

Characterization of wearability and motion artifacts

The CTP method allows an open mesh filamentary serpentine network to be transferred on human skin conformally without any substrate. Therefore, our large-area epidermal electrodes have several unique advantages compared with conventional substrate-supported electrodes. Images in Fig. 4A compare large-area, substrate-free epidermal electrodes with those supported by a 50-μm-thick adhesive polyurethane (PU) substrate on the two forearms of the same participant under various mechanical deformations. It is obvious that, however, the skin deformed, e.g., elbow relaxing, flexing by 90° or rotating by 180°, the substrate-free electrodes imposed no mechanical constraint to the skin, i.e., they were mechanically imperceptible to the skin. In contrast, the PU substrate caused skin wrinkling under various deformations. Even when the skin is fully relaxed, microscopic wrinkles still existed. These wrinkles are attributed to the stiffness mismatch between the PU and the skin as well as the residual strain when transferring the PU sheet to nondevelopable skin surface.

Perspiration and heat dissipating are two other main considerations under wearability. Figure 4B investigates the effects of PU substrate on forearm temperature before and after exercise during the course of three hours. The left and right forearms of the same participant were covered by the substrate-free and PU-supported electrodes, respectively. The detailed experimental procedures are described in Materials and Methods. The top row of Fig. 4B shows the temperature distribution measured by an infrared (IR) camera, and the bottom row plots the full-field averaged temperature with the states labeled as dots. Before transferring anything on the forearm, i.e., state I, normal state, the two forearms had the same temperature of 34.6°C. Ten minutes after both types of electrodes were transferred, i.e., state II before running, the temperature of the right forearm (with PU substrate) was 0.78°C higher than that of the left forearm (substrate-free), owning to the thermal isolation effect of the PU film. The average temperature plot shows that 0.5°C (right forearm) and 1.5°C (left forearm) temperature declines from states I to II, which can be attributed to the evaporation of the conductive gel. After running for 10 min, i.e., state III after running, the evaporation of sweat further cooled the skin down compared with state II, and this cooling is more notable for the substrate-free electrodes on the left forearm. Afterward, the temperature of both forearms recovered gradually as the chart shows, but the temperature difference between the two arms was up to 1.2°C, which caused discernable discomfort to the right arm (*36*, *37*). At state IV, i.e., after removal of both devices, the temperature of the right forearm dropped quickly with the evaporation of accumulated sweat and lastly coincided with the left forearm.

Many works have shown that the impedance of the skin has a negative correlation with perspiration (*3*), which can be transformed to hydration index (*38*). Therefore, we used this parameter to characterize sweat evaporation, as plotted in Fig. 4C. High values of the hydration index indicate more sweat on skin surface. Similar to the thermal experiment, the participant's left and right forearms wore the substrate-free and PU-supported electrodes, respectively. More details of the measurement are provided in Materials and Methods. At state I, the two hydration curves dropped similarly, as the conductive gel was drying. At state II, after applying PU film on the right forearm, the hydration index of the left forearm continued to reduce, whereas that of the right forearm immediately stopped decreasing owing to the impeded evaporation by the PU. At state III, stimulated by high room temperature, the skin started perspiring. However, the hydration index of the left forearm stayed stable because secreting and evaporating of sweat came to a balance without the substrate. As sweat accumulates, the hydration index of the right forearm started to rise. After 20-min running, much sweat was secreted. At the beginning of state IV, the hydration index of both forearms goes up markedly. About 200 min later, the hydration index of the left forearm recovered to the value before exercise. However, the hydration index of the right forearm recovered much slower because of the PU coverage. When evaporation is blocked, some sweat could be reabsorbed by the skin (*39*). Through the hour-long thermal and hydration measurements, it is concluded that large-area epidermal electrodes have to be substrate free to minimize its influence on the natural physiology of the skin.

Biopotentials are typically weak, ranging from several microvolts to several millivolts. Specific to the cut-and-pasted large-area epidermal electrodes without interconnect encapsulation, the signals are further compromised by the dimensionless geometric parameter δ. As a result, the background noise could become problematic. Gel electrodes were used as the gold standard to study the noise level picked up by the epidermal electrodes (*40*). As shown in Fig. 4D, the background noises of substrate-supported and substrate-free electrodes are as low as 5 μV, on par with the commercial gel electrodes (3 M). When the skin was repetitively indented by a glass rod, indentation-induced spikes, which are called motion artifacts, appeared in Fig. 4E and movie S5. Apparently, gel electrodes are the most susceptible to motion artifacts. When subjected to hard indentation, artifacts started to show up in substrate-supported electrodes but still absent from substrate-free electrodes. This observation is consistent with the expectation that the thicker film (the PU membrane in this case) is more susceptible to interface detachment under deformation. We also explored how the dimension and distance of epidermal electrodes affect their sensitivity to motion artifacts. We selected CH 1, CH 6, CH 7, CH 10, and CH 11 of our 16-channel epidermal electrodes as labeled in fig. S2B, whose dimensions are

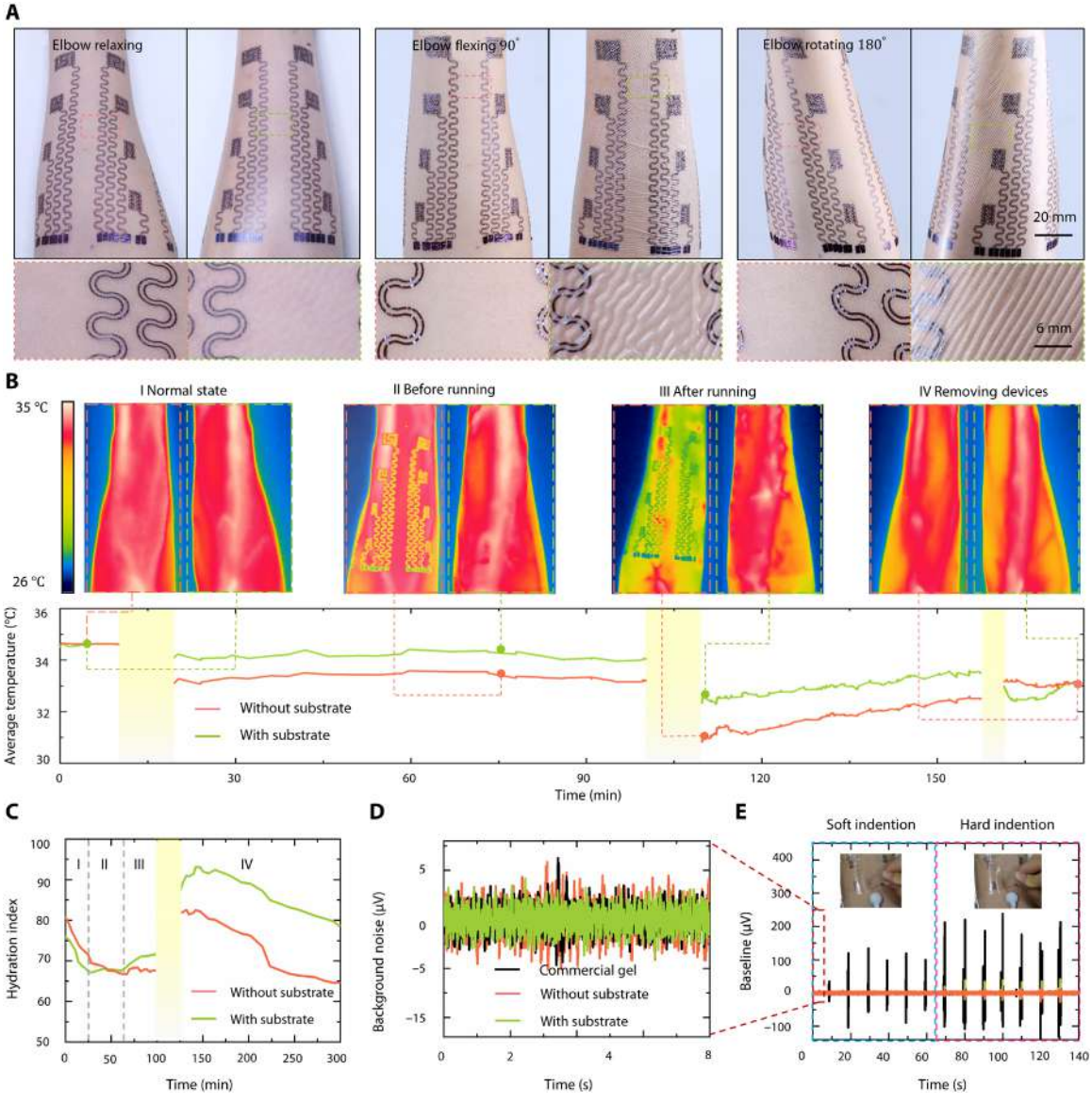

Fig. 4. Mechanical, thermal, and electrical characterization of large-area epidermal electrodes. (**A**) Photographs and corresponding optical micrographs of large-area epidermal electrodes with and without substrate attached on forearm. Scale bars, 1.5 cm. Photo credit: Lin Xiao, State Key Laboratory of Digital Manufacturing Equipment and Technology, Huazhong University of Science and Technology; Flexible Electronics Research Center, Huazhong University of Science and Technology. (**B** and **C**) Temperature and hydration index contrast of electrode-laminated forearm before and after running. Photo credit: Yunzhao Bai, State Key Laboratory of Digital Manufacturing Equipment and Technology, Huazhong University of Science and Technology; Flexible Electronics Research Center, Huazhong University of Science and Technology. (**D**) Background noises of gel electrode and epidermal electrodes with or without substrate. (**E**) Mechanical indentation induced noise in gel electrode and epidermal electrode with or without substrate. Photo credit: Youhua Wang, State Key Laboratory of Digital Manufacturing Equipment and Technology, Huazhong University of Science and Technology; Flexible Electronics Research Center, Huazhong University of Science and Technology.

different as shown in a magnified view in fig. S9. They were attached on the participant's forearm. The participant was told to completely relax his arm muscle to allow the acquisition of noises caused by external motion, which is simulated by skin indentation near CH 7 and CH 11 as indicated by the arrow in fig. S9. EWEs + EEIs and ECBs (see locations in fig. S2A) were directly connected to the positive and negative ports of the data acquisition (DAQ), respectively. Figure S9 labels the potential measured at each electrode induced by skin indentation. It reveals that the electrodes closer to the indentation location recorded higher potentials but the recording was not sensitive to the dimension of the electrode. This is because, at a given location, the average potential over different sizes of an area are similar as long as the electrode is not covering an area of too large potential gradient. Movie S6 further demonstrates that the signals measured by the substrate-free epidermal electrodes are immune from other types of touches. Besides the motion artifacts, we also explored the impact of temperature fluctuations and sweating on background noise, as summarized in the bar chart in fig. S10. It confirms that soft indention, temperature fluctuations, and sweating do not generate notable background noises (noise at 25°C is set

as standard) but the noise induced by hard indentation is approximately four times higher than the rest. The increasing noise from soft indention to hard indention indicates that strenuous exercises should be avoid especially in the case of measuring weak biopotentials such as the sEMG. Therefore, all of our biopotential measurements were conducted under mild to moderate motions. The effect of severe motion on the compensation parameter still remains to be studied.

Applications of the large-area epidermal electrodes on human skin

To demonstrate the diverse capabilities of the large-area epidermal electrodes, we carried out multichannel electrophysiology over the chest, the forearm, and the neck. Owing to the high-quality transfer and high-fidelity sensing, we have achieved cardiac health recording, sign language recognition, and prosthetic control, as well as neck activity classification through sEMG mapping, as shown in Fig. 5. Details on each experiment are provided in Materials and Methods.

American Sign Language (ASL) is the predominant sign language used by the deaf communities in the United States and most of Anglophone Canada. Hence, recognizing ASL via sEMG is beneficial for the deaf to interact with computers and robots. Sixteen-channel sEMG on the forearm was recorded using the electrode layout shown in fig. S2A. We developed a machine-learning algorithm to recognize ASL, and the details of the algorithm are given in Materials and Methods. Figure 5A shows the classification accuracy of 26 alphabets and the rest gesture after verification. Except for alphabet S, other gestures can be classified with very high accuracy (over 96%) and some even 100%. The average classification accuracy is as high as 97.4%. The low accuracy for alphabet S may be attributed to the resemblance to other alphabets, such as A, E, M, and N, which could be improved by means of increasing more channels. Real-time ASL recognition through sEMG was demonstrated by a participant continuously expressing "HELLO," as shown in Fig. 5B. The large-area sEMG electrodes can also serve for the disabled. A left-hand amputee wore that the 16-channel epidermal electrodes could repeatedly control a robotic prosthesis to express his intentions, such as "Rest," "Grab," and "Yes" (Fig. 5C and movie S7).

The large-area epidermal electrodes can also successfully cover the human neck to acquire sEMG. Figure 5 (D to F) shows the sEMG strength maps of neck while performing different tasks, including speaking vowels of A, E, I, and O, swallowing different volumes of water (10 and 60 ml) or chewing on the left/right side, and turning head right/left/forward/back. Various tasks evidently exhibited various spatial distributions of sEMG. The diversity even occurred in the same task (fig. S11, A to C). The asymmetric sEMG maps of turning head left and right (which has been verified using gel electrodes as shown in fig. S12) indicates that the participant's left neck muscles are much stronger than the right ones, which could be attributed to personal habits of muscle use. Speaking vowels generally results in very weak sEMG, while the sEMG associated with head turning could be two orders of magnitudes larger. This complication can be attributed to the complex structure of human neck. There are more than 20 pairs of superficial and deep muscles acting on the cervical vertebrae all the way to the head (*41*). Therefore, mapping neck sEMG has many potential applications, such as rehabilitative speech (*42*), evaluation of normal swallowing functions (*43*), monitoring of musculoskeletal symptoms (*43*), and robot manipulation via head motion (*44*).

The large-area epidermal electrodes also enabled multichannel ECG, the most common cardiac diagnostic tool. Figure S13 (A and B) illustrates ECG of each channel and one representative period of ECG, respectively. ECG of each channel has the typical P, Q, R, S, and T waves but with different amplitudes and shapes, exhibiting the spatial variation, and is therefore used to detect various cardiac diseases from arrhythmias to palpitations.

DISCUSSION

We have successfully designed, fabricated, compensated, and applied a substrate-free tattoo-like electrode system for large-scale epidermal electrophysiology. Highly stretchable and high-area filling-factor electrodes are designed using Peano curves with transformable topology. Dry and free-form cut-and-paste fabrication process is scaling friendly but not capable of interconnect encapsulation. Hence, an electrical compensation theory and the corresponding circuit design have been proposed to eliminate the interference from the EEI. A CTP process is proposed and demonstrated for substrate-free, conformal, and zero-strain transfer to nondevelopable skin surfaces. The breathability of the substrate-free epidermal electrodes is quantified through thermal and hydration characterizations. Applications of these electrodes include multichannel ECG, accurate ASL recognition, and prostheses control, as well as mapping of neck activities. These low-cost but large-area and high-performance epidermal electrodes have paved the way for future large-area epidermal electronics necessary for personnel health/performance management, disease diagnosis, and human-machine interaction.

MATERIALS AND METHODS

Fabrication processes of the large-area tattoo-like electrodes

We developed a modified "cut-and-paste" process, as shown in fig. S14. It began with the lamination of a layer of commercial 1.1-μm-thick transparent PET (polyethylene terephthalate) film (Nanyang Technology, China) on a wetted commercial water-transfer paper (Shanghai Ziyue Digital Technology, China) (fig. S14A). The PET film was metallized by depositing 10-nm-thick chromium and 100-nm-thick gold in sequence after drying the wetted paper. Depending on the resolution requirement of pattern of wires, either the laser machine (LPKF ProtoLaser U4, Germany) or the mechanical cutter (CE6000-40, GRAPHTEC, Japan) was used to pattern the metallic PET film (fig. S14B). The water-transfer paper is composed of an adhesive layer and a supporting paper. The major component of the adhesive layer was identified to be starch that can be hydrolyzed by α-amylase (fig. S14G) and, hence, be used as the sacrificial layer. Hydrolyzation of the sacrificial layer by enzyme is more efficient than the dissolution of polyvinyl alcohol (PVA), while working as the sacrificial layer. The statistics in fig. S14H shows that the efficiency of our method is at least 16 times higher than that of PVA. The patterned metallic PET was detached from the paper via 0.5% α-amylase solution (Tianjin Guangfu Fine Chemical Research Institute, China) at 50° to 70°C (fig. S14C) and then was floating on the water surface. The excessive parts were kept for two reasons. The first reason is to constrain the relative movement of every independent part of the device. The second reason is to prevent in-plane deformation due to the water surface tension. As a temporary substrate, or a donor substrate, for transfer printing, a piece of cloth was

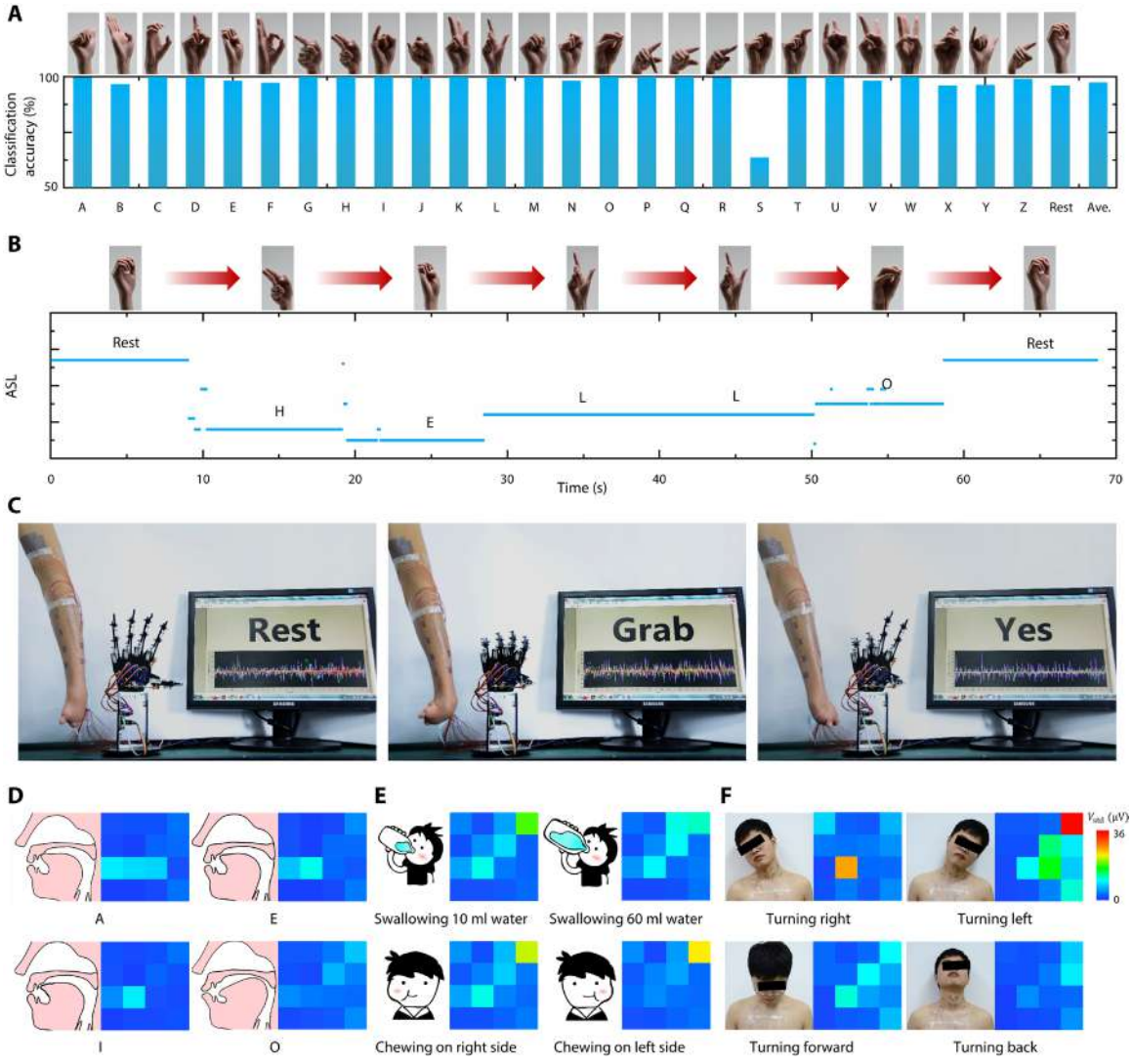

Fig. 5. Various applications of our large-area epidermal electrodes. (**A**) Classification accuracy of 26 American Sign Language (ASL) alphabets and a rest gesture. (**B**) One trial of the continuous recognition of the sign language saying "HELLO". Photo credit: Yunzhao Bai, State Key Laboratory of Digital Manufacturing Equipment and Technology, Huazhong University of Science and Technology; Flexible Electronics Research Center, Huazhong University of Science and Technology. (**C**) A left-hand amputee controlling a robotic prosthetic hand. Photo credit: Youhua Wang and Lang Yin, State Key Laboratory of Digital Manufacturing Equipment and Technology, Huazhong University of Science and Technology; Flexible Electronics Research Center, Huazhong University of Science and Technology. (**D** to **F**) Neck sEMG maps of speaking vowels, swallowing, chewing, and turning head. Photo credit: Youhua Wang, State Key Laboratory of Digital Manufacturing Equipment and Technology, Huazhong University of Science and Technology; Flexible Electronics Research Center, Huazhong University of Science and Technology.

put at the bottom of water. The cloth is only bendable thus satisfies the requirement of CTP mathematics. After the water was pumped out, the floating patterned metallic PET was transferred on the cloth (fig. S14D). After that, the extraneous parts were removed (fig. S14E and movie S8). The interfacial adhesive between the metallic PET and the temporary substrate is extremely weak, so that the removal must be carefully handled to avoid intertwining filamentary electrodes. Once the intertwining happens, the unique feature of ultrastretchability can recover the self-intertwined electrodes, discussed in the first subsection of Results and Discussion. Movie S1 shows one recovery operation. Last, the devices were transfer printed on curvilinear skin surfaces via CTP (fig. S14F) after a thin layer of conductive gel (SignaGel Electrode Gel, USA) with a thickness less than 5 μm was applied to the skin. To protect the attached devices, a diluted conductive gel solution (the weight ratio of deionized water to conductive gel is 4) was sprayed on skin. Meanwhile, the PU-supported electrodes used in the validation experiment and all experiments in Fig. 4 except the sweating characterization were prepared by the method proposed previously (*27*).

Design of epidermal patches used in the validation experiment of the signal compensation theory

The widths of all filaments are 600 μm, and the lengths of filaments in each patch are identical. In patches 1, 2, and 5, the filament length is 242.0 mm; in patches 3 and 4, the filament length is 427.4 mm. Therefore, by definition, the dimensionless geometrical ratio δ is 0.362.

The overall sizes of patches 1, 2, and 5 are 31.4 mm by 30.8 mm, and those of patches 3 and 4 are 50.8 mm by 38.6 mm, shown in fig. S4B.

3D scanning of human body

The participant's forearm, chest, and neck were scanned via a handheld 3D scanner (GScan, ZG Technology Ltd.), the curvilinear surface of the skin was reconstructed, and the Gaussian curvature contour plots were drawn after the data of point position were import into commercial software Geomagic Design X.

The temperature characterization over several hours of the large-area tattoo-like electrodes

The substrate-supported large-area tattoo-like electrodes covered the participant's full right forearm and the substrate-free electrodes were attached on the counterpart location of the left forearm at 10 min. During states I and II, the participant rested in a room under room temperature 25°C. After normal outdoor running (about 10 min at 37°C), the participant rested in the same room at state III. At about 160 min, both of devices were removed. The temperature during the whole process was captured by an IR camera (FLIR T650SC, USA). The PU film is opaque to IR light so that the raw data of electrodes with substrates were corrected to obtain the skin temperature, seen in the Supplementary Materials.

The sweating characterization over several hours of the large-area tattoo-like electrodes

At state I, two substrate-free large-area tattoo-like electrodes were attached on both forearms, and at the beginning of state II, a piece of adhesive PU film wrapped the right forearm, mimicking the PU-supported electrodes. The room temperature was 25°C at states I and II. At state III, the room temperature was raised to about 30°C. At 105 min, the participant was asked to run for 20 min. After that, the participant rested in the room with 25°C. During the whole process, an impedance analyzer (E4980a, Keysight) was used to measure the impedance between channel 10 and channel 11.

The connection to the external DAQ device

The stable connection to external DAQ device is of critical importance to minimize contact resistance, especially for weak biosignals. As shown in fig. S15, the low-melting alloy of melting temperature 45°C, at which the human skin can endure, was used to weld connecting pads and thin copper foils (10 μm). The copper foil was then connected to a high-resolution DAQ card (PXIe-4302, National Instruments) via soft shielded wires (the maximum diameter is 300 μm). The shielded wires could greatly suppress 50-Hz noise. Tegaderm film (3M Ltd.) thermally isolated the melting alloy, and double-sided tapes (4902, VHB, 3M Ltd.) reinforced the welding of low-melting alloy.

Recognition of ASL and control of prosthesis hand

The acquisition modules and the compensation modules were transferred over the full forearm and on the upper arm, respectively, as shown in fig. S16A. The participant repeated every ASL alphabet 10 times. At first, the filtered signals were divided by δ of each channel to get V_{EWE} after the elimination of baseline wandering and a power noise of 50 Hz via a high-pass filter with the cutoff of 5 Hz and a notch filter of 50 Hz. By the way, all electrophysiological data in this paper were filtered with a high-pass filter with the cutoff of 5 Hz and a notch filter of 50 Hz. Then, two typical time-domain features, including mean absolute value and root mean square, and one typical frequency-domain feature, mean frequency, were extracted and imported to a built-in neural network–based pattern recognition in MATLAB. After trained with half of the data, the network was validated with the remaining and then used to carry out the continuous recognitions or the manipulation of a robotic hand.

sEMG contour of neck activities

The acquisition modules were transferred over the neck, and the compensation modules were transferred on the upper right back, where the muscles kept still (fig. S16B). SD was used to characterize the strength of neck activities, after sEMG data were filtered and divided with δ of each channel to get V_{EWE} as the same as the former experiments.

Multichannel ECG acquisition

The acquisition modules covered the chest, and the compensation modules were on the lower right abdomen, where electrophysiological signals were stable (fig. S16C). The ECG signals were filtered and divided by δ of each channel to get V_{EWE} as the same as the former experiments.

SUPPLEMENTARY MATERIALS

Supplementary material for this article is available at http://advances.sciencemag.org/cgi/content/full/6/43/eabd0996/DC1

View/request a protocol for this paper from *Bio-protocol*.

REFERENCES AND NOTES

1. M. Seeber, L.-M. Cantonas, M. Hoevels, T. Sesia, V. Visser-Vandewalle, C. M. Michel, Subcortical electrophysiological activity is detectable with high-density EEG source imaging. *Nat. Commun.* **10**, 753 (2019).
2. M. Zhu, B. Yu, W. Yang, Y. Jiang, L. Lu, Z. Huang, S. Chen, G. Li, Evaluation of normal swallowing functions by using dynamic high-density surface electromyography maps. *Biomed. Eng. Online* **16**, 133 (2017).
3. Y. Wang, Y. Qiu, S. K. Ameri, H. Jang, Z. Dai, Y. Huang, N. Lu, Low-cost, μm-thick, tape-free electronic tattoo sensors with minimized motion and sweat artifacts. *npj Flex. Electron.* **2**, 6 (2018).
4. C. Dai, Y. Zheng, X. Hu, Estimation of muscle force based on neural drive in a hemispheric stroke survivor. *Front. Neurol.* **9**, 187 (2018).
5. L. Cai, C. Wang, Carbon nanotube flexible and stretchable electronics. *Nanoscale Res. Lett.* **10**, 320 (2015).
6. X. An, G. K. Stylios, A hybrid textile electrode for electrocardiogram (ECG) measurement and motion tracking. *Materials (Basel)* **11**, 1887 (2018).
7. Y. M. Chi, T.-P. Jung, G. Cauwenberghs, Dry-contact and noncontact biopotential electrodes: Methodological review. *IEEE Rev. Biomed. Eng.* **3**, 106–119 (2010).
8. D. J. Bracken, G. Ornelas, T. P. Coleman, P. A. Weissbrod, High-density surface electromyography: A visualization method of laryngeal muscle activity. *Laryngoscope* **129**, 2347–2353 (2019).
9. C. Yang, Z. Suo, Hydrogel ionotronics. *Nat. Rev. Mater.* **3**, 125–142 (2018).
10. C. Keplinger, J.-Y. Sun, C. C. Foo, P. Rothemund, G. M. Whitesides, Z. Suo, Stretchable, transparent, ionic conductors. *Science* **341**, 984–987 (2013).
11. H.-J. Kim, K. Sim, A. Thukral, C. Yu, Rubbery electronics and sensors from intrinsically stretchable elastomeric composites of semiconductors and conductors. *Sci. Adv.* **3**, e1701114 (2017).
12. D.-H. Kim, N. Lu, R. Ma, Y.-S. Kim, R.-H. Kim, S. Wang, J. Wu, S. M. Won, H. Tao, A. Islam, K. J. Yu, T.-i. Kim, R. Chowdhury, M. Ying, L. Xu, M. Li, H.-J. Chung, H. Keum, M. McCormick, P. Liu, Y.-W. Zhang, F. G. Omenetto, Y. Huang, T. Coleman, J. A. Rogers, Epidermal electronics. *Science* **333**, 838–843 (2011).
13. J. A. Fan, W.-H. Yeo, Y. Su, Y. Hattori, W. Lee, S.-Y. Jung, Y. Zhang, Z. Liu, H. Cheng, L. Falgout, M. Bajema, T. Coleman, D. Gregoire, R. J. Larsen, Y. Huang, J. A. Rogers, Fractal design concepts for stretchable electronics. *Nat. Commun.* **5**, 3266 (2014).
14. Y. Zhang, H. Fu, S. Xu, J. A. Fan, K.-C. Hwang, J. Jiang, J. A. Rogers, Y. Huang, A hierarchical computational model for stretchable interconnects with fractal-inspired designs. *J. Mech. Phys. Solids* **72**, 115–130 (2014).

15. J. C. Yang, J. Mun, S. Y. Kwon, S. Park, Z. Bao, S. Park, Electronic skin: Recent progress and future prospects for skin-attachable devices for health monitoring, robotics, and prosthetics. *Adv. Mater.* **31**, 1904765 (2019).
16. Y. Kim, A. Chortos, W. Xu, Y. Liu, J. Y. Oh, D. Son, J. Kang, A. M. Foudeh, C. Zhu, Y. Lee, S. Niu, J. Liu, R. Pfattner, Z. Bao, T.-W. Lee, A bioinspired flexible organic artificial afferent nerve. *Science* **360**, 998–1003 (2018).
17. L. Tian, B. Zimmerman, A. Akhtar, K. J. Yu, M. Moore, J. Wu, R. J. Larsen, J. W. Lee, J. Li, Y. Liu, B. Metzger, S. Qu, X. Guo, K. E. Mathewson, J. A. Fan, J. Cornman, M. Fatina, Z. Xie, Y. Ma, J. Zhang, Y. Zhang, F. Dolcos, M. Fabiani, G. Gratton, T. Bretl, L. J. Hargrove, P. V. Braun, Y. Huang, J. A. Rogers, Large-area MRI-compatible epidermal electronic interfaces for prosthetic control and cognitive monitoring. *Nat. Biomed. Eng.* **3**, 194–205 (2019).
18. J. Heikenfeld, A. Jajack, J. Rogers, P. Gutruf, L. Tian, T. Pan, R. Li, M. Khine, J. Kim, J. Wang, J. Kim, Wearable sensors: Modalities, challenges, and prospects. *Lab Chip* **18**, 217–248 (2018).
19. C. Majidi, R. S. Fearing, Adhesion of an elastic plate to a sphere. *Proc. R. Soc. A Math. Phys. Eng. Sci.* **464**, 1309–1317 (2008).
20. L. Wang, S. Qiao, S. Kabiri Ameri, H. Jeong, N. Lu, A thin elastic membrane conformed to a soft and rough substrate subjected to stretching/compression. *J. Appl. Mech.* **84**, 111003 (2017).
21. H. C. Ko, G. Shin, S. Wang, M. P. Stoykovich, J. W. Lee, D.-H. Kim, J. S. Ha, Y. Huang, K.-C. Hwang, J. A. Rogers, Curvilinear electronics formed using silicon membrane circuits and elastomeric transfer elements. *Small* **5**, 2703–2709 (2009).
22. Y. M. Song, Y. Xie, V. Malyarchuk, J. Xiao, I. Jung, K.-J. Choi, Z. Liu, H. Park, C. Lu, R.-H. Kim, R. Li, K. B. Crozier, Y. Huang, J. A. Rogers, Digital cameras with designs inspired by the arthropod eye. *Nature* **497**, 95–99 (2013).
23. B. Le Borgne, S. Liu, X. Morvan, S. Crand, R. A. Sporea, N. Lu, M. Harnois, Water transfer printing enhanced by water-induced pattern expansion: Toward large-area 3D electronics. *Adv. Mater. Technol.* **4**, 1800600 (2019).
24. K. Sim, S. Chen, Z. Li, Z. Rao, J. Liu, Y. Lu, S. Jang, F. Ershad, J. Chen, J. Xiao, C. Yu, Three-dimensional curvy electronics created using conformal additive stamp printing. *Nat. Electron.* **2**, 471–479 (2019).
25. Y. Xu, B. Sun, Y. Ling, Q. Fei, Z. Chen, X. Li, P. Guo, N. Jeon, S. Goswami, Y. Liao, S. Ding, Q. Yu, J. Lin, G. Huang, Z. Yan, Multiscale porous elastomer substrates for multifunctional on-skin electronics with passive-cooling capabilities. *Proc. Natl. Acad. Sci. U.S.A.* **117**, 205–213 (2020).
26. A. Miyamoto, S. Lee, N. F. Cooray, S. Lee, M. Mori, N. Matsuhisa, H. Jin, L. Yoda, T. Yokota, A. Itoh, M. Sekino, H. Kawasaki, T. Ebihara, M. Amagai, T. Someya, Inflammation-free, gas-permeable, lightweight, stretchable on-skin electronics with nanomeshes. *Nat. Nanotechnol.* **12**, 907–913 (2017).
27. S. Yang, Y.-C. Chen, L. Nicolini, P. Pasupathy, J. Sacks, B. Su, R. Yang, D. Sanchez, Y.-F. Chang, P. Wang, D. Schnyer, D. Neikirk, N. Lu, "Cut-and-Paste" manufacture of multiparametric epidermal sensor systems. *Adv. Mater.* **27**, 6423–6430 (2015).
28. A. Gallina, T. Vieira, Territory and fiber orientation of vastus medialis motor units: A surface electromyography investigation. *Muscle Nerve* **52**, 1057–1065 (2015).
29. T. Yamamoto, Y. Yamamoto, Analysis for the change of skin impedance. *Med. Biol. Eng. Comput.* **15**, 219–227 (1977).
30. K. Nomizu, Kinematics and differential geometry of submanifolds. *Tohoku Math. J.* **30**, 623–637 (1978).
31. M. Raffaelli, J. Bohr, S. Markvorsen, in *Bridges 2016: Mathematics, Music, Art, Architecture, Education, Culture* (Tessellations Publishing, 2016), pp. 457–460.
32. O. S. Kim, in *2013 IEEE Antennas and Propagation Society International Symposium (APSURSI)* (IEEE, 2013), pp. 776–777.
33. L. Xiao, C. Zhu, W. Xiong, Y. Huang, Z. Yin, The conformal design of an island-bridge structure on a non-developable surface for stretchable electronics. *Micromachines (Basel)* **9**, 392 (2018).
34. S. Kabiri Ameri, R. Ho, H. Jang, L. Tao, Y. Wang, L. Wang, D. M. Schnyer, D. Akinwande, N. Lu, Graphene electronic tattoo sensors. *ACS Nano* **11**, 7634–7641 (2017).
35. W.-H. Yeo, Y.-S. Kim, J. Lee, A. Ameen, L. Shi, M. Li, S. Wang, R. Ma, S. H. Jin, Z. Kang, Y. Huang, J. A. Rogers, Multifunctional epidermal electronics printed directly onto the skin. 25, 2773–2778 (2013).
36. E. R. Nadel, J. W. Mitchell, J. A. J. Stolwijk, Differential thermal sensitivity in the human skin. *Pflugers Arch.* **340**, 71–76 (1973).
37. I. Darian-Smith, K. O. Johnson, Thermal sensibility and thermoreceptors. *J. Invest. Dermatol.* **69**, 146–153 (1977).
38. D. Salter, in *Skin Bioengineering* (Karger Publishers, 1998), vol. 26, pp. 38–47.
39. K. Sato, in *Reviews of Physiology, Biochemistry and Pharmacology*, R. H. Adrian, E. Helmreich, H. Holzer, R. Jung, K. Kramer, O. Krayer, R. J. Linden, F. Lynen, P. A. Miescher, J. Piiper, H. Rasmussen, A. E. Renold, U. Trendelenburg, K. Ullrich, W. Vogt, A. Weber, Eds. (Springer Berlin Heidelberg, 1977), vol. 79, pp. 51–131.
40. M. A. Lopez-Gordo, D. Sanchez-Morillo, F. P. Valle, Dry EEG electrodes. *Sensors* **14**, 12847–12870 (2014).
41. J.-S. Blouin, G. P. Siegmund, M. G. Carpenter, J. T. Inglis, Neural control of superficial and deep neck muscles in humans. *J. Neurophysiol.* **98**, 920–928 (2007).
42. C. E. Stepp, J. T. Heaton, R. G. Rolland, R. E. Hillman, Neck and face surface electromyography for prosthetic voice control after total laryngectomy. *IEEE Trans. Neural Syst. Rehabil. Eng.* **17**, 146–155 (2009).
43. C. M. Sommerich, S. M. Joines, V. Hermans, S. D. Moon, Use of surface electromyography to estimate neck muscle activity. *J. Electromyogr. Kinesiol.* **10**, 377–398 (2000).
44. N. Rudigkeit, M. Gebhard, AMiCUS—A head motion-based interface for control of an assistive robot. *Sensors* **19**, 2836 (2019).
45. T. Widlund, S. Yang, Y.-Y. Hsu, N. Lu, Stretchability and compliance of freestanding serpentine-shaped ribbons. *Int. J. Solids Struct.* **51**, 4026–4037 (2014).
46. P. Chappuis, P. Pittet, E. Jéquier, Heat storage regulation in exercise during thermal transients. *J. Appl. Physiol.* **40**, 384–392 (1976).

Acknowledgments: Y.W. thanks J. Sun and Z. Guo, LPKF employees, for laser patterning. **Funding:** This research was supported by the National Natural Science Foundation of China (grant nos. 51925503 and 51635007) and the Program for HUST Academic Frontier Youth Team. N.L. acknowledges the support by US NSF (grant no. 1738293). The general characterization facilities are provided by the Flexible Electronics Manufacturing Laboratory in Comprehensive Experiment Center for Advanced Manufacturing Equipment and Technology at HUST. **Ethics statement:** The Institutional Review Board of Tongji Hospital, Tongji Medical College, Huazhong University of Science and Technology approved the protocol of the study [permit number (2018) IEC (S512), Wuhan, China]. All procedures performed in studies involving human participants were in accordance with the ethical standards of the institutional and/or national research committee and with the 1964 Helsinki declaration and its later amendments or comparable ethical standards. **Author contributions:** The signal compensation theory and CTP were developed by Y.W., Y.H., and N.L. Processes and experiments were designed by Y.W., Y.Z., Y.B., Y.H., and N.L. and performed by Y.W., Y.H., L.Y., Y.B., Y.Z., C.H., Z.Ya., H.W., J.M., Y.S., P.D., S.Z., T.D., Z.L., J.R., and L.X. FEM was performed by Y.W., S.L., Y.H., and C.H. Y.H. and N.L. supervised the overall research. N.L., Y.W., Y.H., S.L, L.W., L.Y., Y.B., and Z.Yi. contributed to the writing of the manuscript. **Competing interests:** Y.H., Y.W., and Z.Yi. are inventors on a patent related to this work filed by Huazhong University of Science and Technology (no. CN201710240754.8, filed 13 April 2017). Y.H., Y.W., T.D., Y.Z., and Z.Yi. are inventors on a patent application related to this work filed by Huazhong University of Science and Technology (no. CN108634936A, filed 10 May 2018). The authors declare that they have no other competing interests. **Data and materials availability:** All data needed to evaluate the conclusions in the paper are present in the paper and/or the Supplementary Materials. Additional data related to this paper may be requested from the authors.

Submitted 2 June 2020
Accepted 9 September 2020
Published 23 October 2020
10.1126/sciadv.abd0996

Citation: Y. Wang, L. Yin, Y. Bai, S. Liu, L. Wang, Y. Zhou, C. Hou, Z. Yang, H. Wu, J. Ma, Y. Shen, P. Deng, S. Zhang, T. Duan, Z. Li, J. Ren, L. Xiao, Z. Yin, N. Lu, Y. Huang, Electrically compensated, tattoo-like electrodes for epidermal electrophysiology at scale. *Sci. Adv.* **6**, eabd0996 (2020).

Electrically compensated, tattoo-like electrodes for epidermal electrophysiology at scale

Youhua Wang, Lang Yin, Yunzhao Bai, Siyi Liu, Liu Wang, Ying Zhou, Chao Hou, Zhaoyu Yang, Hao Wu, Jiaji Ma, Yaoxin Shen, Pengfei Deng, Shuchang Zhang, Tangjian Duan, Zehan Li, Junhui Ren, Lin Xiao, Zhouping Yin, Nanshu Lu and YongAn Huang

Sci Adv **6** (43), eabd0996.
DOI: 10.1126/sciadv.abd0996

Science Advances
AAAS

advances.sciencemag.org/cgi/content/full/6/43/eabd0996/DC1

Supplementary Materials for

Electrically compensated, tattoo-like electrodes for epidermal electrophysiology at scale

Youhua Wang, Lang Yin, Yunzhao Bai, Siyi Liu, Liu Wang, Ying Zhou, Chao Hou, Zhaoyu Yang, Hao Wu, Jiaji Ma, Yaoxin Shen, Pengfei Deng, Shuchang Zhang, Tangjian Duan, Zehan Li, Junhui Ren, Lin Xiao, Zhouping Yin, Nanshu Lu*, YongAn Huang*

*Corresponding author. Email: yahuang@hust.edu.cn (Y.H.); nanshulu@utexas.edu (N.L.)

Published 23 October 2020, *Sci. Adv.* **6**, eabd0996 (2020)
DOI: 10.1126/sciadv.abd0996

The PDF file includes:

Other Supplementary Material for this manuscript includes the following:

(available at advances.sciencemag.org/cgi/content/full/6/43/eabd0996/DC1)

Note S1. Signal compensation theory

The continuous form of the distributed-parameter model can be written as:

$$V = \frac{\int \frac{E}{z} dl}{\int \frac{1}{z} dl} \tag{S1}$$

where E is the electrical potential of voltage source and z is the unit cross-sectional area impedance. z of a uniform specimen of materials is

$$\mathrm{z} = \rho_{\mathrm{resistivity}} t = ZA \tag{S2}$$

where $\rho_{\mathrm{resistivity}}$ is the electrical resistivity; t is the length of the specimen and herein is the thickness of stratum corneum; Z is the total impedance of the specimen; A is the cross-sectional area of the specimen.

When the electrode is uncompensated, the acquired voltage is:

$$V_{uncompensated} = \frac{\int_0^{L_1+L_2} \frac{E}{z} dl}{\int_0^{L_1+L_2} \frac{1}{z} dl} = V_{EWE} \frac{\int_{L_1}^{L_1+L_2} \frac{1}{z} dl}{\int_0^{L_1+L_2} \frac{1}{z} dl} + V_{EEI} \frac{\int_0^{L_1} \frac{1}{z} dl}{\int_0^{L_1+L_2} \frac{1}{z} dl} \tag{S3}$$

$$V_{EWE} = \frac{\int_{L_1}^{L_1+L_2} \frac{E}{z} dl}{\int_{L_1}^{L_1+L_2} \frac{1}{z} dl} \tag{S4}$$

$$V_{EEI} = \frac{\int_0^{L_1} \frac{E}{z} dl}{\int_0^{L_1} \frac{1}{z} dl} \tag{S5}$$

where L_1 and L_2 are the length of EEI and the EWE, respectively. V_{EWE} and V_{EEI} are the voltages acquired by the EWE and EEI, respectively. $\int_{L_1}^{L_1+L_2} \frac{1}{z} dl \,/\, \int_0^{L_1+L_2} \frac{1}{z} dl$ and $\int_0^{L_1} \frac{1}{z} dl \,/\, \int_0^{L_1+L_2} \frac{1}{z} dl$ are weight factors of V_{EWE} and V_{EEI}, respectively.

The acquired voltage in ECB is:

$$V_{ECB} = V_{EEI} \tag{S6}$$

By simply subtracting V_{ECB} from $V_{uncompensated}$, the differential voltage is:

$$V_{partially\_compensated} = V_{EWE}\frac{\int_{L_1}^{L_1+L_2}\frac{1}{z}dl}{\int_{0}^{L_1+L_2}\frac{1}{z}dl} - V_{EEI}\frac{\int_{L_1}^{L_1+L_2}\frac{1}{z}dl}{\int_{0}^{L_1+L_2}\frac{1}{z}dl} \quad \text{(S7)}$$

It is evident that such method cannot completely eliminate V_{EEI}. $V_{uncompensated} - V_{ECB}$ is therefore named partially compensation method.

To thoroughly eliminate the signals of EEI, we assume there exists another electrode with length of L_3 that connects to ECB, so that the corresponding voltage of ECB becomes:

$$\tilde{V}_{ECB} = V_{new\_electrode}\frac{\int_{L_1}^{L_1+L_3}\frac{1}{z}dl}{\int_{0}^{L_1+L_3}\frac{1}{z}dl} + V_{EEI}\frac{\int_{0}^{L_1}\frac{1}{z}dl}{\int_{0}^{L_1}\frac{1}{z}dl+\int_{L_1}^{L_1+L_3}\frac{1}{z}dl} \quad \text{(S8)}$$

$$V_{new\_electrode} = \frac{\int_{0}^{L_3}\frac{E_{New\_Electrode}}{z}dl}{\int_{0}^{L_3}\frac{1}{z}dl} \quad \text{(S9)}$$

V_{EEI} is successfully cancelled by $V_{uncompensated} - \tilde{V}_{ECB}$ if (1) $E_{new\_electrode} \equiv 0$, that is, where the electrical potential in dermis layers and muscles beneath this electrode equals to zero, (2) $L_3 = L_2$, and (3) the corresponding unit cross-sectional area impedance z of the new electrode and EWE is the same. This new electrode is called the epidermal compensation electrode (ECE). The impedance of ECE is:

$$Z = \frac{1}{\int_{L_1}^{L_1+L_2}\frac{1}{z}dl} \quad \text{(S10)}$$

The compensated signal by subtracting $\tilde{V}_{ECB}$ from $V_{uncompensated}$ is

$$V_{compensated} = V_{EWE}\frac{\int_{L_1}^{L_1+L_2}\frac{1}{z}dl}{\int_{0}^{L_1+L_2}\frac{1}{z}dl} \quad \text{(S11)}$$

If z is identical everywhere, the compensated signal is

$$V_{compensated} = V_{EWE}\frac{L_2}{L_1+L_2} \quad \text{(S12)}$$

We assume z is identical everywhere for simplicity in the following discussion.

More practically, considering the potential difference between the ECEs and EGE, though both them are required to be neighbor. The compensated voltage can be expressed as:

$$V(\Delta\vec{\boldsymbol{l}}) = \frac{L_2}{L_1+L_2} V_{EWE} - \frac{\int_{L_1}^{L_1+L_2} E_{compensation\_module} dl}{L_1+L_2} \quad \text{(S13)}$$

Where $E_{compensation\_module}$ is the potential beneath ECEs, and $\Delta\vec{\boldsymbol{l}}$ is a vector representing the distance between the ECEs and the EGE.

$E_{compensation_module}$can be further got using Taylor series:

$$E_{compensation\_module} \approx -\nabla E_{EGE} \cdot \Delta\vec{\boldsymbol{l}} \quad \text{(S14)}$$

Where ∇E_{EGE} is potential gradient beneath the EGE. Either decreasing ∇E_{EGE} or shortening $\Delta\vec{\boldsymbol{l}}$ can weaken the negative effect of $E_{compensation\_module}$.

Specific to the validation experiment, the voltage of Channel 1 is:

$$V_{CH1} = \frac{\int_0^{L_{chest}} (E_1 - E_2) dl}{L_{chest}} \quad \text{(S15)}$$

Where E_1 and E_2 are the bio-potential beneath the positive and negative electrodes, respectively, L_{chest} is the length of EWEs on chest.

The voltage of Channel 2 is:

$$V_{CH2} = \frac{\int_0^{L_{arm}+L_{chest}} (E_1 - E_2) dl}{L_{arm}+L_{chest}} \quad \text{(S16)}$$

Where L_{arm} is the length of AIWs on forearms.

The partially compensated voltage (switch off) is:

$$V_p = \frac{L_{chest}}{L_{arm}+L_{chest}} V_{CH1} + \frac{L_{chest}}{L_{arm}+L_{chest}} \int_0^{L_{arm}} (E_2 - E_1) dl \quad \text{(S17)}$$

The compensated voltage (switch on) is:

$$V_c = \frac{L_{chest}}{L_{arm}+L_{chest}} V_{CH1} \quad \text{(S18)}$$

Note S2. Maximum coverage ratio calculation of serpentine structures

Analogous to the definitions in *(45)*, w is the ribbon width, R the arc radius, θ the arc angle. Generally, the coverage ratio may be expressed as:

$$\sigma = \frac{(\pi+2\theta)\frac{w}{R}}{2cos\theta(2\,sin\,\theta+2+\frac{w}{R})} \tag{S19}$$

The coverage ratio reaches maximum once the neighboring ribbons contact. In this case, θ is:

$$\theta = arccos(\frac{1}{2}+\frac{w}{4R}) \tag{S20}$$

Substituting equation (S20) into equation (S19), the maximum coverage ratio is:

$$\sigma_{max} = \frac{\left(\pi+2arccos(\frac{1}{2}+\frac{w}{4R})\right)\frac{w}{R}}{(1+\frac{w}{2R})(2\sqrt{1-\left(\frac{1}{2}+\frac{w}{4R}\right)^2}+2+\frac{w}{R})} \tag{S21}$$

σ_{max} is only up to the ratio of the ribbon width to the arc radius.

Note S3. Pearson correlation coefficient (PCC)

PCC is a measure of the linear correlation between two variables *X* and *Y,* used to characterize SNR.

$$\rho = \frac{E[(X-\mu_X)(Y-\mu_Y)]}{\sigma_X\sigma_Y} \tag{S22}$$

Where σ_X and σ_Y are the standard deviations of *X* and *Y* respectively, μ_X and μ_Y are the mean of *X* and *Y* respectively, and *E* is the expectation.

Note S4. Theory of Cartan development

Given a curve $\tilde{\boldsymbol{\gamma}}$ embedded within a general surface $\tilde{S}$ and another general surface *S* moves along $\tilde{\boldsymbol{\gamma}}$ as pure rolling. The motion curve on S is $\boldsymbol{\gamma}$. The two surfaces contact at point $\boldsymbol{X}$ on surface $\tilde{S}$ and at $\boldsymbol{x}$ on surface S, representing undeformed configuration and deformed configuration, respectively.

After transfer printing, the relation between $\boldsymbol{X}$ and $\boldsymbol{x}$ can be written as

$$\boldsymbol{x} = \boldsymbol{AX} + \boldsymbol{p} \tag{S23}$$

In which $\boldsymbol{x}$ and $\boldsymbol{X}$ are the position vectors of a point on $\tilde{\boldsymbol{\gamma}}$ and $\boldsymbol{\gamma}$ respectively; $\boldsymbol{A}$ is rotation matrix and $\boldsymbol{p}$ a translation vector. Take derivative of equation (S23) with time *t*, the velocity can be obtained

$$\dot{\boldsymbol{x}} = \dot{\boldsymbol{A}}\boldsymbol{X} + \boldsymbol{A}\dot{\boldsymbol{X}} + \dot{\boldsymbol{p}} \tag{S24}$$

Considering this motion is a pure rolling, equation (S24) must satisfy

$$\dot{\boldsymbol{A}}\boldsymbol{X} + \dot{\boldsymbol{p}} = \boldsymbol{0} \tag{S25}$$

Hence, equation (S24) will be

$$\dot{\boldsymbol{x}} = \boldsymbol{A}\dot{\boldsymbol{X}} \tag{S26}$$

Noting that the rotation matrix satisfies $\boldsymbol{A}\boldsymbol{A}^T = \boldsymbol{I}$, so we can get

$$|d\boldsymbol{x}| = |d\boldsymbol{X}| \tag{S27}$$

The Darboux frame $\{\boldsymbol{e}, \boldsymbol{h}, \boldsymbol{n}\}$ of $\tilde{\boldsymbol{S}}$ satisfies

$$\begin{pmatrix} \frac{d\boldsymbol{e}}{dt} \\ \frac{d\boldsymbol{h}}{dt} \\ \frac{d\boldsymbol{n}}{dt} \end{pmatrix} = |\dot{\boldsymbol{x}}| \begin{pmatrix} 0 & \kappa_g & \kappa_n \\ -\kappa_g & 0 & \tau_g \\ -\kappa_n & -\tau_g & 0 \end{pmatrix} \begin{pmatrix} \boldsymbol{e} \\ \boldsymbol{h} \\ \boldsymbol{n} \end{pmatrix} \tag{S28}$$

where κ_g, κ_n, τ_g are Geodesic curvature, normal curvature, and relative torsion of $\tilde{\boldsymbol{\gamma}}$, respectively. The Darboux frame $\{\boldsymbol{E}, \boldsymbol{H}, \boldsymbol{N}\}$ of S satisfies

$$\begin{pmatrix} \frac{d\boldsymbol{E}}{dt} \\ \frac{d\boldsymbol{H}}{dt} \\ \frac{d\boldsymbol{N}}{dt} \end{pmatrix} = |\dot{X}| \begin{pmatrix} 0 & \kappa_G & \kappa_N \\ -\kappa_G & 0 & \tau_G \\ -\kappa_N & -\tau_G & 0 \end{pmatrix} \begin{pmatrix} \boldsymbol{E} \\ \boldsymbol{H} \\ \boldsymbol{N} \end{pmatrix} \tag{S29}$$

where κ_G, κ_N, τ_G are Geodesic curvature, normal curvature, and relative torsion of $\boldsymbol{\gamma}$, respectively. Similar to equation (S26), two Darboux frames must satisfy

$$\begin{pmatrix} \boldsymbol{e} \\ \boldsymbol{h} \\ \boldsymbol{n} \end{pmatrix} = \boldsymbol{A} \begin{pmatrix} \boldsymbol{E} \\ \boldsymbol{H} \\ \boldsymbol{N} \end{pmatrix} \tag{S30}$$

Take derivative of equation (S30) and using equation (S29) and the equation $\dot{\boldsymbol{A}}\boldsymbol{A}^{\boldsymbol{T}}\boldsymbol{r} = \boldsymbol{\omega} \times \boldsymbol{r}$, we can get

$$\boldsymbol{\omega} \times \boldsymbol{e} = |\dot{\boldsymbol{x}}|\{(\kappa_G - \kappa_g)\boldsymbol{h} + (\kappa_N - \kappa_n)\boldsymbol{n}\} \tag{S31}$$

$$\boldsymbol{\omega} \times \boldsymbol{h} = |\dot{\boldsymbol{x}}|\{(\kappa_g - \kappa_G)\boldsymbol{e} + (\tau_G - \tau_g)\boldsymbol{n}\} \tag{S32}$$

$$\boldsymbol{\omega} \times \boldsymbol{n} = |\dot{\boldsymbol{x}}|\{(\kappa_n - \kappa_N)\boldsymbol{e} + (\tau_g - \tau_G)\boldsymbol{h}\} \tag{S33}$$

where $\boldsymbol{\omega}$ is a vector of the angular velocity. Combining equation (S31)-(S33), $\boldsymbol{\omega}$ can be expressed as

$$\boldsymbol{\omega} = |\dot{\boldsymbol{x}}|\{(\tau_G - \tau_g)\boldsymbol{e} + (\kappa_n - \kappa_N)\boldsymbol{h} + (\kappa_G - \kappa_g)\boldsymbol{n}\} \tag{S34}$$

No spinning allowed in normal direction of surface at the contact point in the pure rolling motion, hence, we can get another significant corollary:

$$\kappa_g = \kappa_G \tag{S35}$$

Katsumi Nomizu firstly revealed that $\tilde{\boldsymbol{\gamma}}$ is the Cartan development of $\boldsymbol{\gamma}$*(30)*.

The above discussion does not have specific requirements for both curvy surfaces.

The maximum strain of a beam with thickness of h transferred on S as a Cartan curve is

$$\varepsilon_{max} = \frac{h}{2}\kappa_N \tag{S36}$$

Let us consider $\tilde{S}$ as a fixed plane and S as a sphere with radius of R. In this case, the maximum strain of a beam on the sphere is

$$\varepsilon_{max} \equiv \frac{h}{2R} \tag{S37}$$

Note S5. Correcting the temperature data of the electrodes with substrates

For the PU film is opaque to infrared light, the infrared camera only captures the temperature of top surface of the PU film. The PU film is about 55 μm thick, hence it is reasonably to consider the problem as one-dimensional steady-state heat conduction problem.

$$\frac{\partial^2 T}{\partial y^2} = 0 \tag{S38}$$

By solving differential equation (S38), skin temperature is

$$T_{skin} = T_{outer} + \frac{q\delta}{\lambda} \tag{S39}$$

In which, T_{skin} and T_{outer} are the temperature of skin and the top surface of the PU film respectively, δ and λ are the thickness and the thermal conductivity of the PU film respectively, and q is the heat loss power of human body*(46)*.

Note S6. Definitions of main abbreviations

ECE = epidermal compensation electrode;

ECB = epidermal compensation branch;

EEI = exposed epidermal interconnect;

EWE = epidermal working electrode;

EGE = epidermal ground electrode;

CPT = Cartan transfer printing;

DPT = direct transfer printing;

ECG = electrocardiography;

sEMG = surface electromyography;

EEG = electroencephalography;

SNR = signal-to-noise ratio;

PCC = Pearson correlation coefficient.

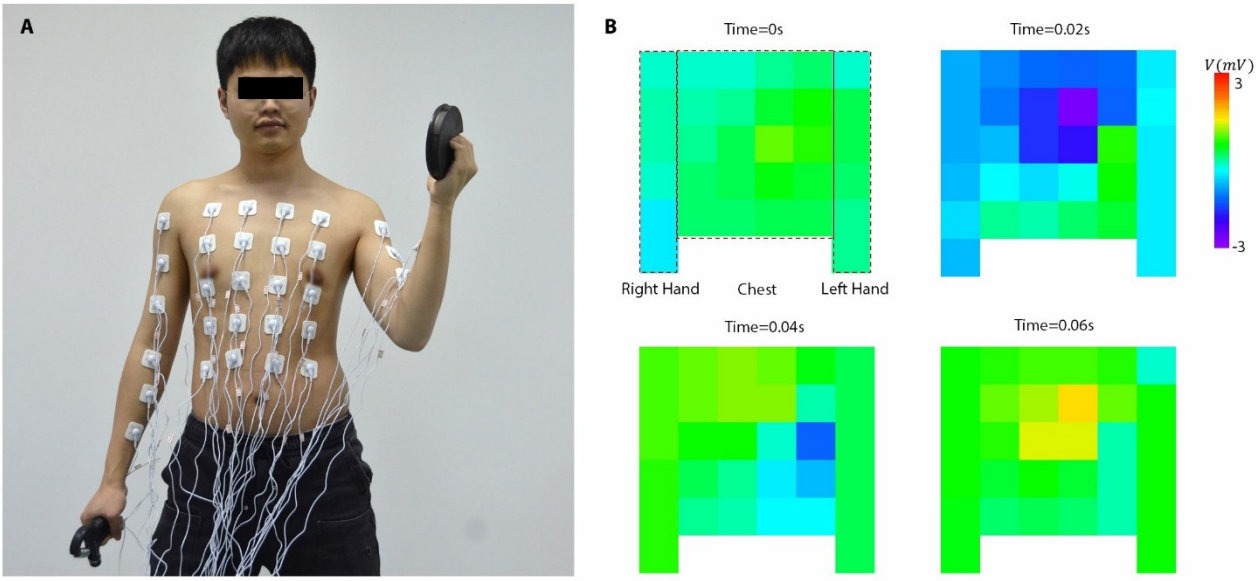

Fig. S1. A body-scale measurement of electrophysiological signals. (**A**) Photo of experiment. There were 34 electrodes on subject's body, including 32 working electrodes, one ground electrode, and one reference electrode. 20 of the working electrodes were on the chest and abdomen, and 12 of them were on both arms. The reference electrode and ground electrode were on the lower back. (**B**) Electrophysiological contour plots changing over time.

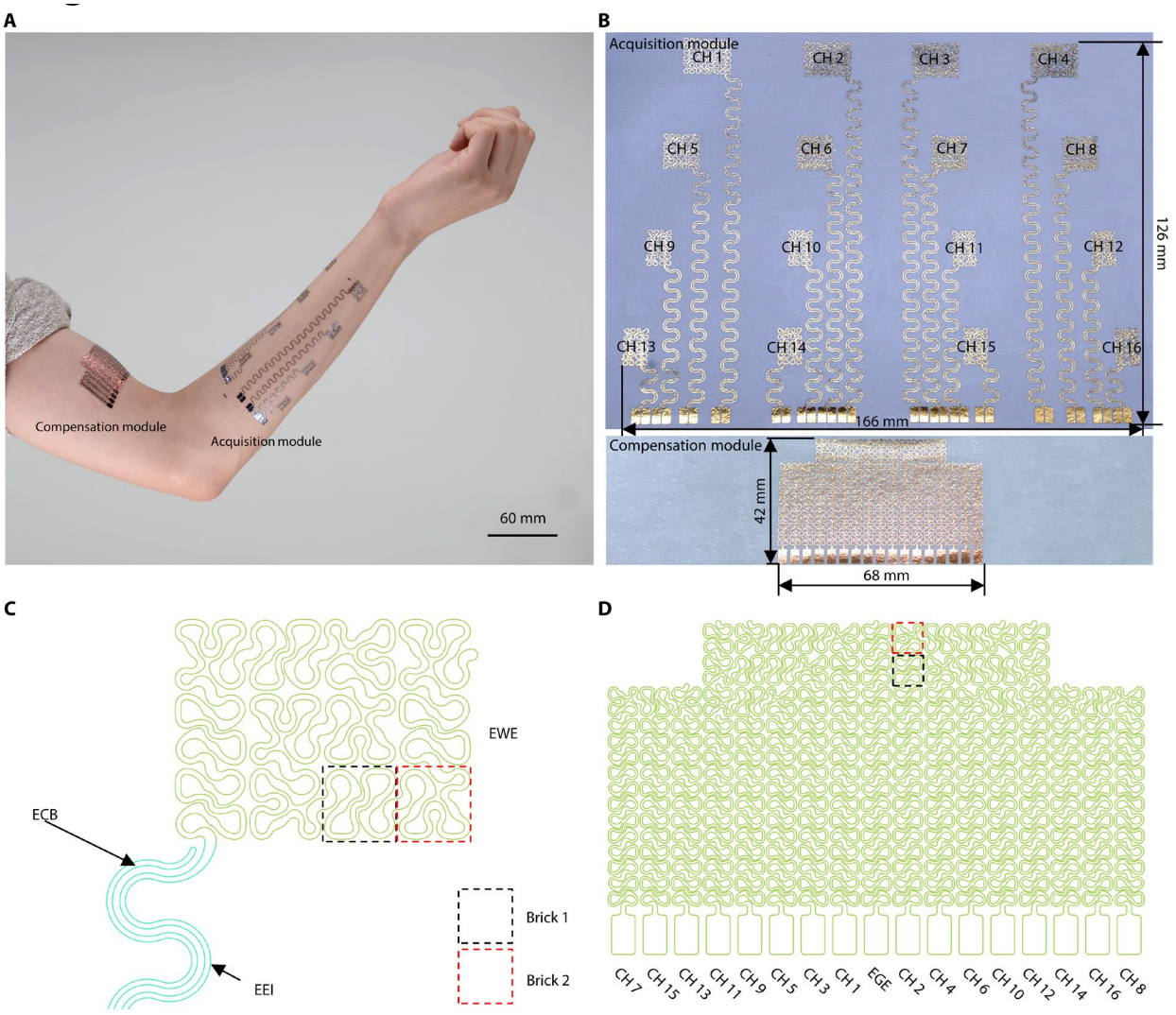

Fig. S2. Design of epidermal electrodes at scale. (**A**) The acquisition module and the compensation module were laminated on forearm and upper arm, respectively. (**B**) Dimensions of the acquisition module and the compensation module. (**C**) A representative EWE is composed of two bricks. The ECB is parallel to the EEI. Both ECB and EEI have the same width of 300 μm. (**D**) the order of ECEs in the compensation module.

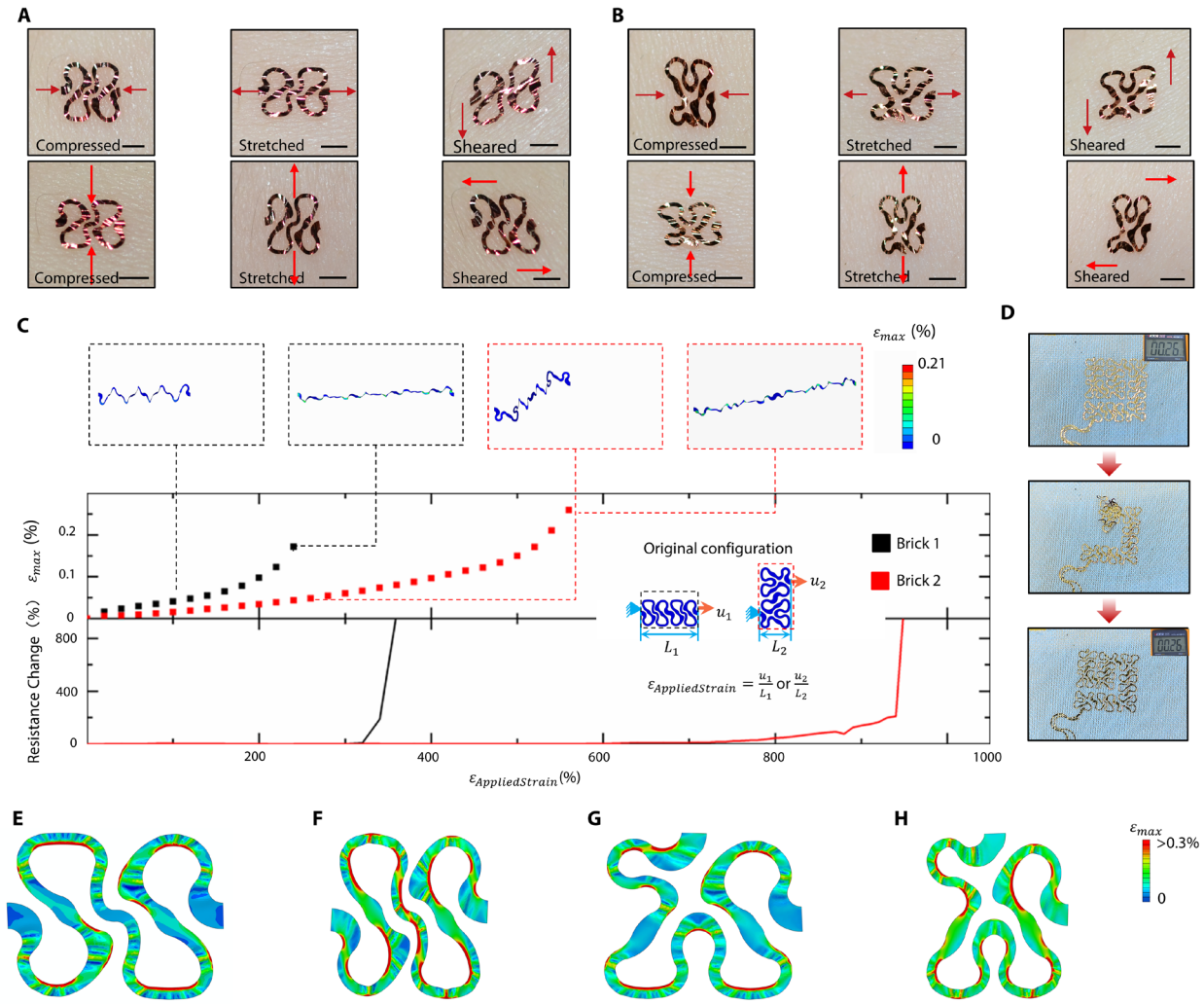

Fig. S3. Mechanical characterization of two bricks. (**A**) Brick 1 and (**B**) Brick 2 under various deformation of skin. (**C**) Maximum principle strain and electrical resistance change with respect to applied strain. The freestanding Brick 1 and Brick 2 can be stretched up to 240% applied strain and 560% applied strain, respectively. (**D**) One example of recovering an electrode owing to the ultra stretchability of two bricks. The inserted photographs were the electrical resistance of the electrode. FEM simulation of uniaxial tension along horizontal direction (**E**)(**F**) or along vertical direction (**G**)(**H**).

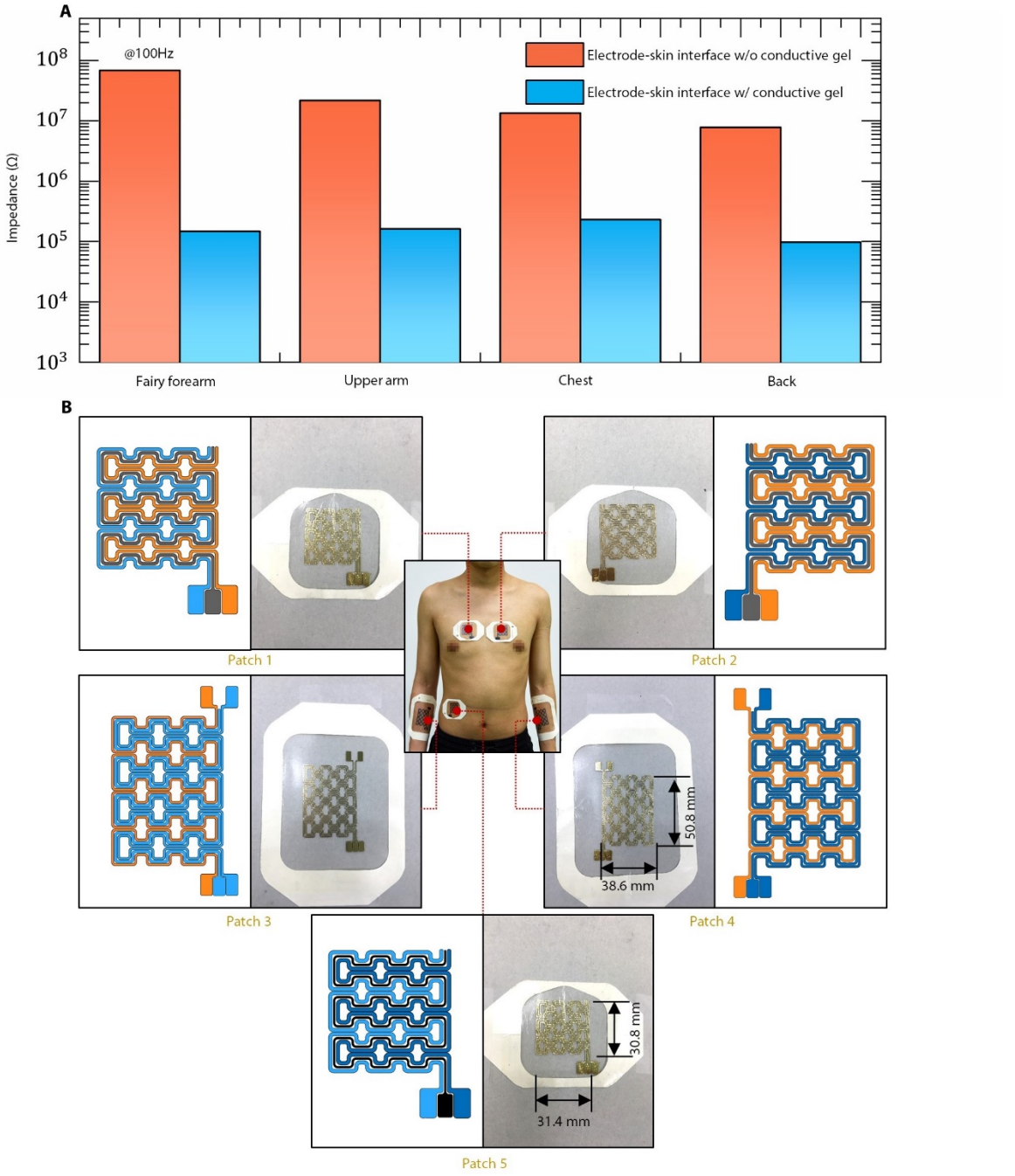

Fig. S4. The validation experiment. (**A**) The impact of commercial conductive gel on electrode-skin impedance. The applied frequency is 100 Hz. (**B**) Sketches and photographs of patches.

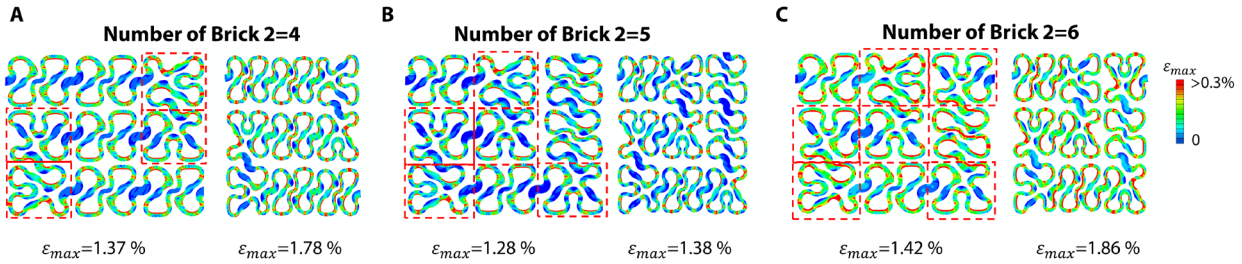

Fig. S5. FEM results of skin-supported electrodes with different numbers of Brick 2 subjected to 18% tensile strain in the horizontal (left panel) and vertical (right panel) directions. The dashed boxes are Brick 2.

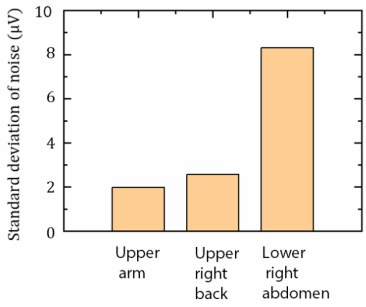

Fig. S6. The noise from compensation itself. The noise was recorded by measuring the potential difference between EGE and CH 8 in Fig. S2D on different body parts.

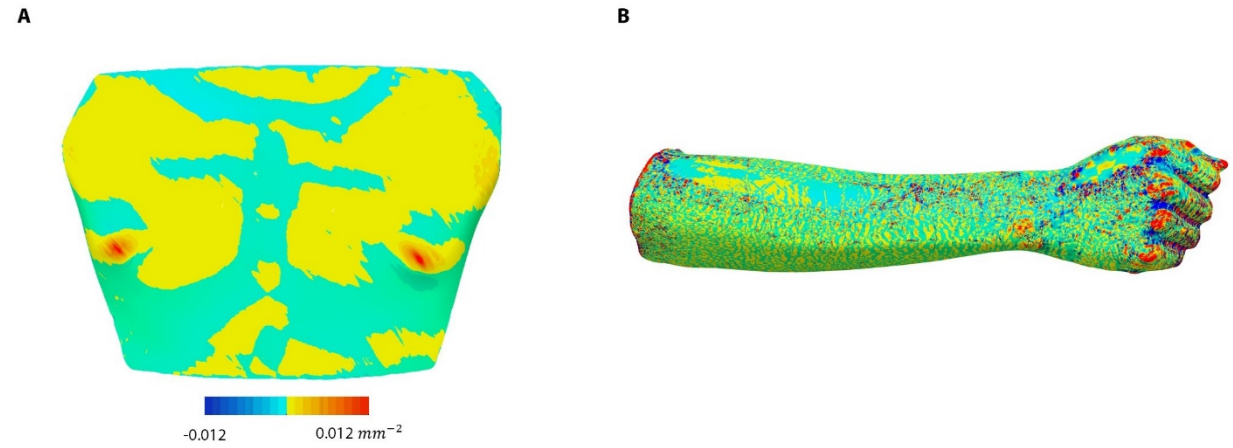

Fig. S7. Gaussian curvature distributions of different body parts. (**A**) the whole chest and (**B**) the forearm with hand.

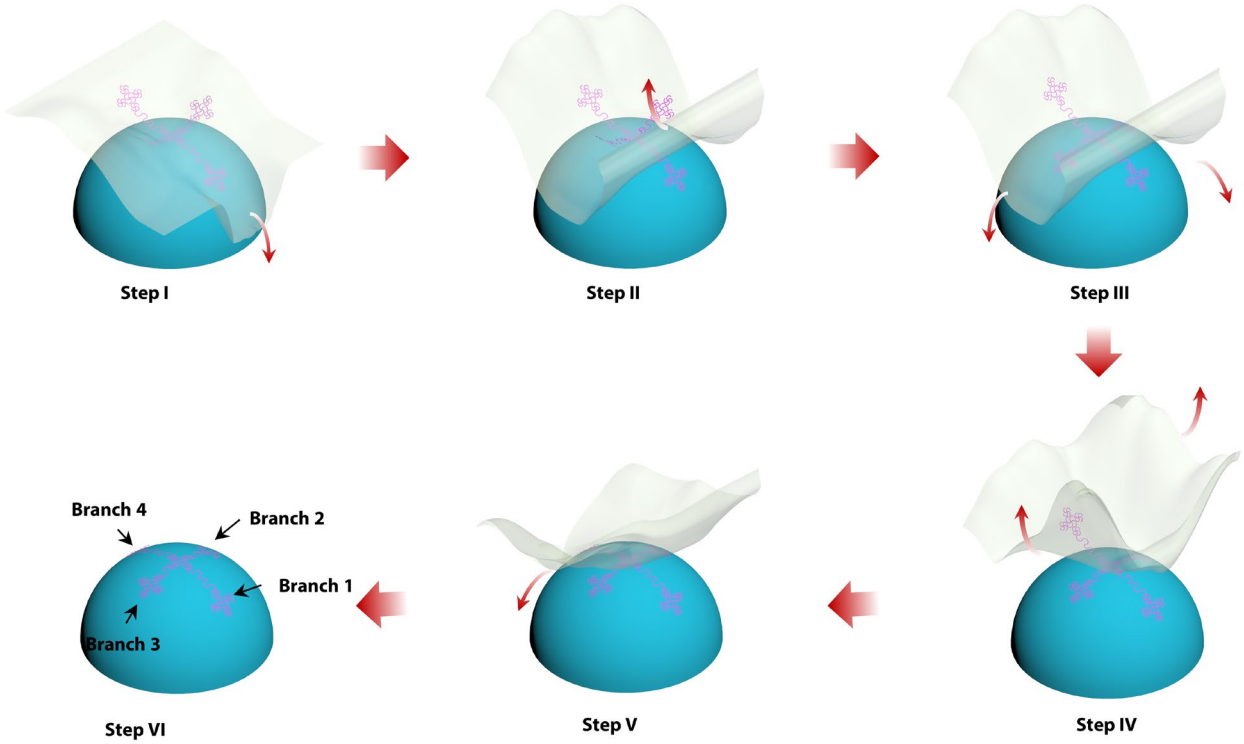

Fig. S8. Step-by-step schematics for the CTP process. (**Step I**) The cloth covered by Branch 1 was laminated on an adhesive hemispherical shell. (**Step II**) Such part of cloth after dried by napkins was detached and Branch 1 was left on the shell. (**Step III**) – (**Step VI**) Similar to Step I and Step II, all of other branches were successively transferred on the shell.

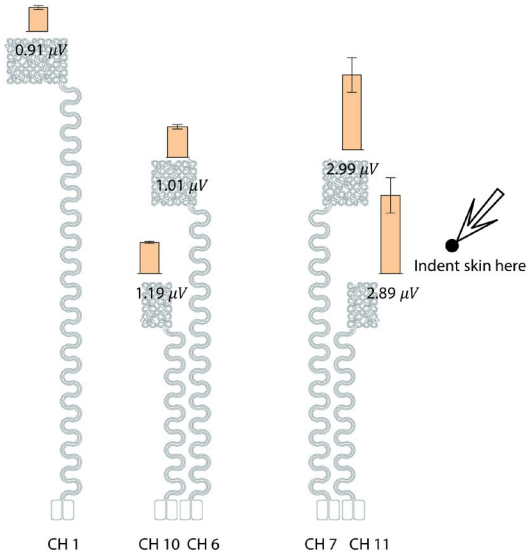

Fig. S9. Indenting skin to explore the relationship between electrode dimensions/inter-distance and motion artifacts.

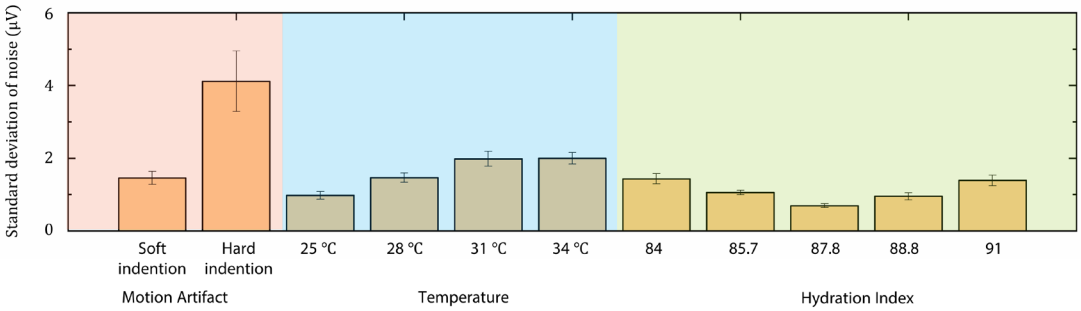

Fig. S10. The motion artifacts under various activities.

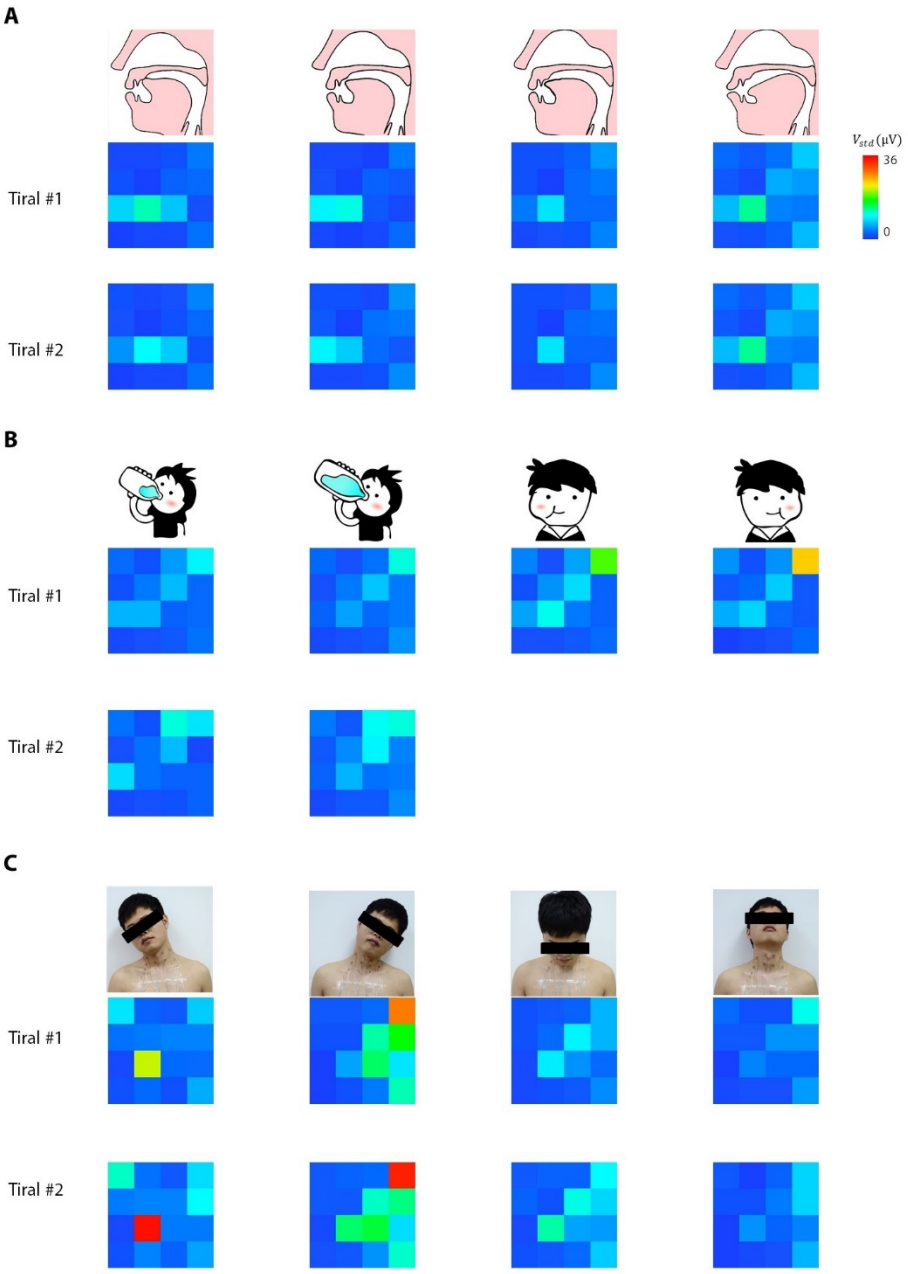

Fig. S11. SEMG strength maps of neck with different types of activities. (**A**) Speaking vowels, (**B**) swallowing/chewing and (**C**) turning head.

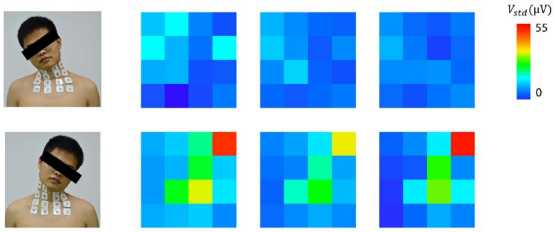

Fig. S12. Neck sEMG maps of turning heads captured by 3M gel electrodes.

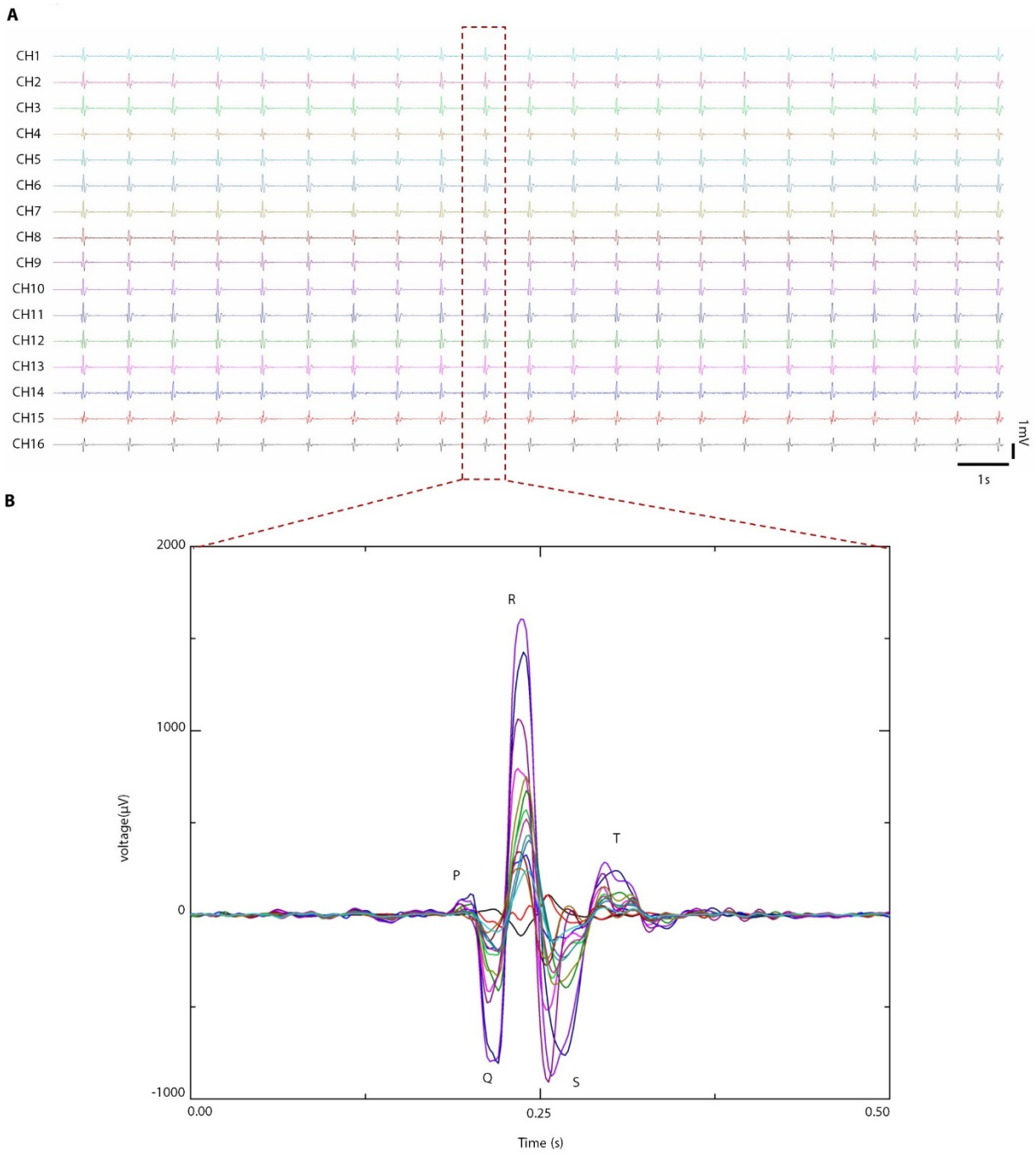

Fig. S13. Multi-channel ECG recorded by epidermal electrodes at scale. (**A**) 16-channel ECG signals. (**B**) Representative zoomed-in ECG signals.

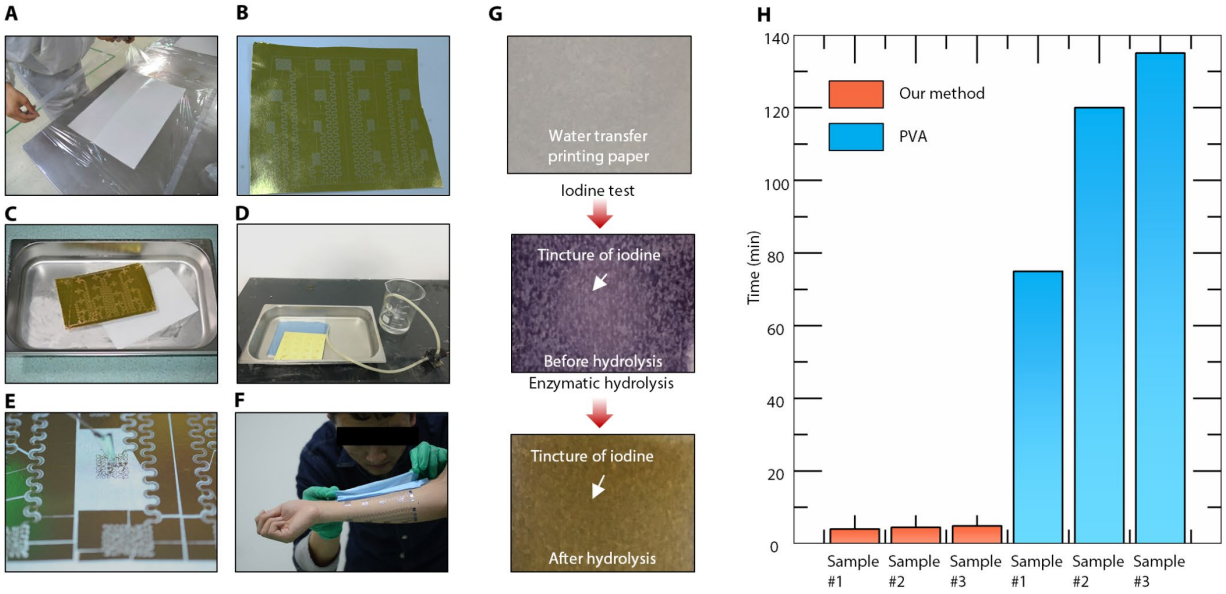

Fig. S14. modified 'Cut-and-Paste' fabrication processes of the large-area tattoo-like electrodes. (**A**) A layer of commercial 1.1-μm-thick transparent PET film was laminated on water-transfer paper. (**B**) The metallic PET was patterned by either a laser cutter or a mechanical cutter. (**C**) The patterned metallic PET was detached from the paper and was floating on water. (**D**) the patterned metallic PET was transferred on cloth by pumping water out. (**E**) The extraneous parts were removed by a sharp tweezer. (**F**) The large-area tattoo-like electrodes were transferred. (**G**) Component identification of the sacrificial layer. (**H**) Time consumption using water-soluble PVA or enzyme-hydrolysis starch as sacrificial layers.

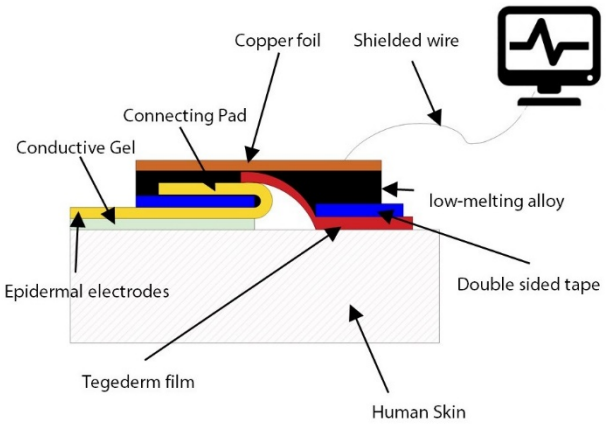

Fig. S15. A method of stable connection.

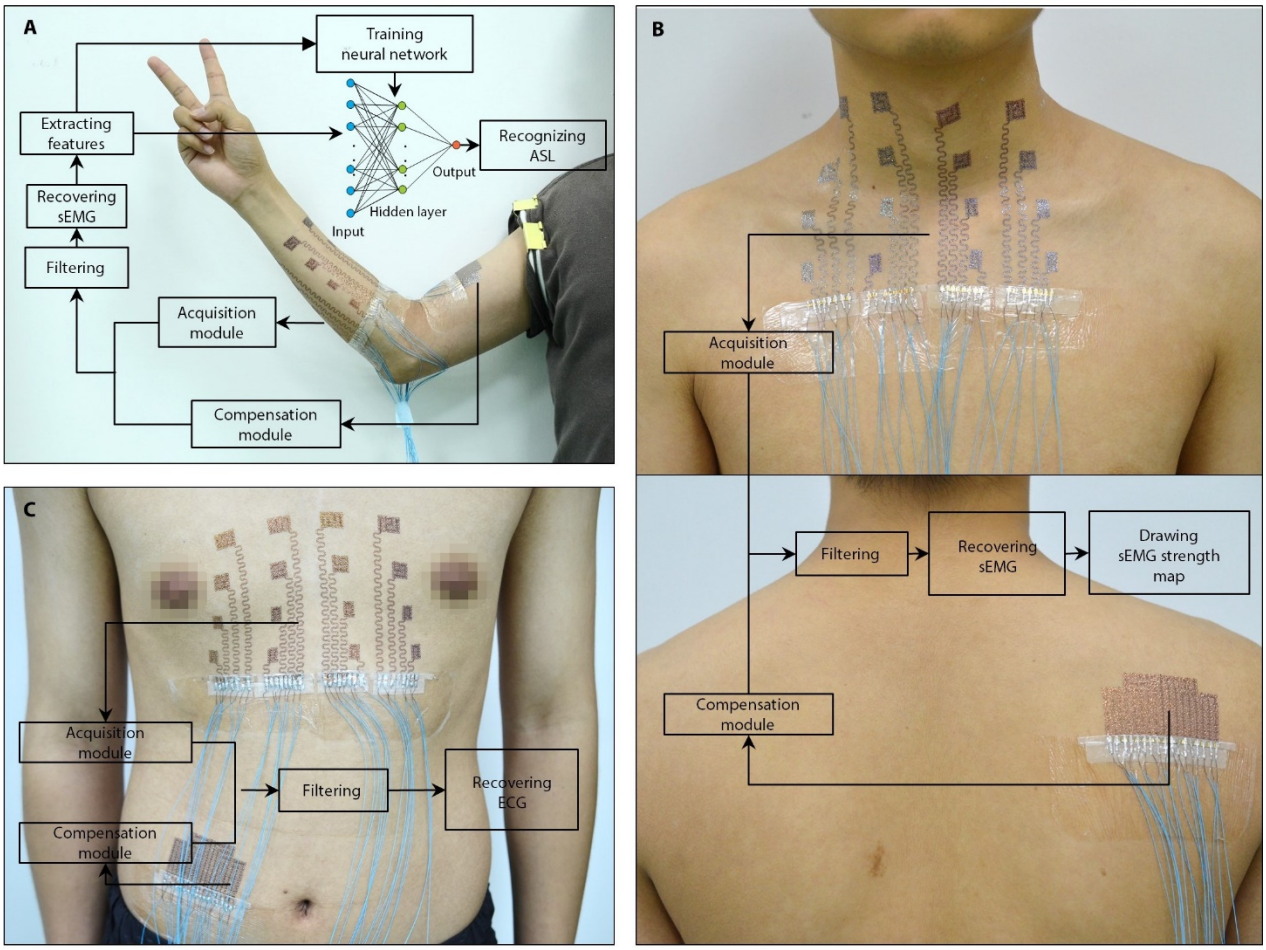

Fig. S16. The entire processes of three application scenarios. (**A**) ASL training and recognition. (**B**) neck activities. (**C**) ECG.

Movie S1. Recovering a self-intertwining filamentary electrode.

Movie S2. Experimental validation of signal compensation theory.

Movie S3. A curved filament transferred on a transparent hemisphere surface by CTP.

Movie S4. A serpentine device transferred on a transparent hemisphere by CTP.

Movie S5. The effect of motion artifact on signal robustness.

Movie S6. Substrate-free electrodes endured severe touches.

Movie S7. A left-hand amputee wearing an epidermal electrode controlled a robotic prosthesis.

Movie S8. The extraneous parts were carefully removed by a sharp tweezer.

Photo credits

Photograph Names	Photographer Names	Photographer Institutions
Figure S1	Youhua Wang	State Key Laboratory of Digital Manufacturing Equipment and Technology, Huazhong University of Science and Technology; Flexible Electronics Research Center, Huazhong University of Science and Technology
Figure S2A	Yunzhao Bai	
Figure S2B	Lin Xiao	
Figure S3A, S3B	Lin Xiao	
Figure S3D	Youhua Wang	
Figure S4B	Youhua Wang	
Figure S11C	Youhua Wang	
Figure S12	Youhua Wang	
Figure S14B, S14C, S14D, S14G	Youhua Wang	
Figure S14A, S14F	Lang Yin	
Figure S14E	Ying Zhou, Youhua Wang	
Figure S16A	Yunzhao Bai	
Figure S16B, S16C	Youhua Wang	

REFERENCES AND NOTES

1. M. Seeber, L.-M. Cantonas, M. Hoevels, T. Sesia, V. Visser-Vandewalle, C. M. Michel, Subcortical electrophysiological activity is detectable with high-density EEG source imaging. *Nat. Commun.* **10**, 753 (2019).
2. M. Zhu, B. Yu, W. Yang, Y. Jiang, L. Lu, Z. Huang, S. Chen, G. Li, Evaluation of normal swallowing functions by using dynamic high-density surface electromyography maps. *Biomed. Eng. Online* **16**, 133 (2017).
3. Y. Wang, Y. Qiu, S. K. Ameri, H. Jang, Z. Dai, Y. Huang, N. Lu, Low-cost, μm-thick, tape-free electronic tattoo sensors with minimized motion and sweat artifacts. *npj Flex. Electron.* **2**, 6 (2018).
4. C. Dai, Y. Zheng, X. Hu, Estimation of muscle force based on neural drive in a hemispheric stroke survivor. *Front. Neurol.* **9**, 187 (2018).
5. L. Cai, C. Wang, Carbon nanotube flexible and stretchable electronics. *Nanoscale Res. Lett.* **10**, 320 (2015).
6. X. An, G. K. Stylios, A hybrid textile electrode for electrocardiogram (ECG) measurement and motion tracking. *Materials (Basel)* **11**, 1887 (2018).
7. Y. M. Chi, T.-P. Jung, G. Cauwenberghs, Dry-contact and noncontact biopotential electrodes: Methodological review. *IEEE Rev. Biomed. Eng.* **3**, 106–119 (2010).
8. D. J. Bracken, G. Ornelas, T. P. Coleman, P. A. Weissbrod, High-density surface electromyography: A visualization method of laryngeal muscle activity. *Laryngoscope* **129**, 2347–2353 (2019).
9. C. Yang, Z. Suo, Hydrogel ionotronics. *Nat. Rev. Mater.* **3**, 125–142 (2018).
10. C. Keplinger, J.-Y. Sun, C. C. Foo, P. Rothemund, G. M. Whitesides, Z. Suo, Stretchable, transparent, ionic conductors. *Science* **341**, 984–987 (2013).
11. H.-J. Kim, K. Sim, A. Thukral, C. Yu, Rubbery electronics and sensors from intrinsically stretchable elastomeric composites of semiconductors and conductors. *Sci. Adv.* **3**, e1701114 (2017).
12. D.-H. Kim, N. Lu, R. Ma, Y.-S. Kim, R.-H. Kim, S. Wang, J. Wu, S. M. Won, H. Tao, A. Islam, K. J. Yu, T.-i. Kim, R. Chowdhury, M. Ying, L. Xu, M. Li, H.-J. Chung, H. Keum, M. McCormick, P. Liu, Y.-W. Zhang, F. G. Omenetto, Y. Huang, T. Coleman, J. A. Rogers, Epidermal electronics. *Science* **333**, 838–843 (2011).

13. J. A. Fan, W.-H. Yeo, Y. Su, Y. Hattori, W. Lee, S.-Y. Jung, Y. Zhang, Z. Liu, H. Cheng, L. Falgout, M. Bajema, T. Coleman, D. Gregoire, R. J. Larsen, Y. Huang, J. A. Rogers, Fractal design concepts for stretchable electronics. *Nat. Commun.* **5**, 3266 (2014).
14. Y. Zhang, H. Fu, S. Xu, J. A. Fan, K.-C. Hwang, J. Jiang, J. A. Rogers, Y. Huang, A hierarchical computational model for stretchable interconnects with fractal-inspired designs. *J. Mech. Phys. Solids* **72**, 115–130 (2014).
15. J. C. Yang, J. Mun, S. Y. Kwon, S. Park, Z. Bao, S. Park, Electronic skin: Recent progress and future prospects for skin-attachable devices for health monitoring, robotics, and prosthetics. *Adv. Mater.* **31**, 1904765 (2019).
16. Y. Kim, A. Chortos, W. Xu, Y. Liu, J. Y. Oh, D. Son, J. Kang, A. M. Foudeh, C. Zhu, Y. Lee, S. Niu, J. Liu, R. Pfattner, Z. Bao, T.-W. Lee, A bioinspired flexible organic artificial afferent nerve. *Science* **360**, 998–1003 (2018).
17. L. Tian, B. Zimmerman, A. Akhtar, K. J. Yu, M. Moore, J. Wu, R. J. Larsen, J. W. Lee, J. Li, Y. Liu, B. Metzger, S. Qu, X. Guo, K. E. Mathewson, J. A. Fan, J. Cornman, M. Fatina, Z. Xie, Y. Ma, J. Zhang, Y. Zhang, F. Dolcos, M. Fabiani, G. Gratton, T. Bretl, L. J. Hargrove, P. V. Braun, Y. Huang, J. A. Rogers, Large-area MRI-compatible epidermal electronic interfaces for prosthetic control and cognitive monitoring. *Nat. Biomed. Eng.* **3**, 194–205 (2019).
18. J. Heikenfeld, A. Jajack, J. Rogers, P. Gutruf, L. Tian, T. Pan, R. Li, M. Khine, J. Kim, J. Wang, J. Kim, Wearable sensors: Modalities, challenges, and prospects. *Lab Chip* **18**, 217–248 (2018).
19. C. Majidi, R. S. Fearing, Adhesion of an elastic plate to a sphere. *Proc. R. Soc. A Math. Phys. Eng. Sci.* **464**, 1309–1317 (2008).
20. L. Wang, S. Qiao, S. Kabiri Ameri, H. Jeong, N. Lu, A thin elastic membrane conformed to a soft and rough substrate subjected to stretching/compression. *J. Appl. Mech.* **84**, 111003 (2017).
21. H. C. Ko, G. Shin, S. Wang, M. P. Stoykovich, J. W. Lee, D.-H. Kim, J. S. Ha, Y. Huang, K.-C. Hwang, J. A. Rogers, Curvilinear electronics formed using silicon membrane circuits and elastomeric transfer elements. *Small* **5**, 2703–2709 (2009).

22. Y. M. Song, Y. Xie, V. Malyarchuk, J. Xiao, I. Jung, K.-J. Choi, Z. Liu, H. Park, C. Lu, R.-H. Kim, R. Li, K. B. Crozier, Y. Huang, J. A. Rogers, Digital cameras with designs inspired by the arthropod eye. *Nature* **497**, 95–99 (2013).

23. B. Le Borgne, S. Liu, X. Morvan, S. Crand, R. A. Sporea, N. Lu, M. Harnois, Water transfer printing enhanced by water-induced pattern expansion: Toward large-area 3D electronics. *Adv. Mater. Technol.* **4**, 1800600 (2019).

24. K. Sim, S. Chen, Z. Li, Z. Rao, J. Liu, Y. Lu, S. Jang, F. Ershad, J. Chen, J. Xiao, C. Yu, Three-dimensional curvy electronics created using conformal additive stamp printing. *Nat. Electron.* **2**, 471–479 (2019).

25. Y. Xu, B. Sun, Y. Ling, Q. Fei, Z. Chen, X. Li, P. Guo, N. Jeon, S. Goswami, Y. Liao, S. Ding, Q. Yu, J. Lin, G. Huang, Z. Yan, Multiscale porous elastomer substrates for multifunctional on-skin electronics with passive-cooling capabilities. *Proc. Natl. Acad. Sci. U.S.A.* **117**, 205–213 (2020).

26. A. Miyamoto, S. Lee, N. F. Cooray, S. Lee, M. Mori, N. Matsuhisa, H. Jin, L. Yoda, T. Yokota, A. Itoh, M. Sekino, H. Kawasaki, T. Ebihara, M. Amagai, T. Someya, Inflammation-free, gas-permeable, lightweight, stretchable on-skin electronics with nanomeshes. *Nat. Nanotechnol.* **12**, 907–913 (2017).

27. S. Yang, Y.-C. Chen, L. Nicolini, P. Pasupathy, J. Sacks, B. Su, R. Yang, D. Sanchez, Y.-F. Chang, P. Wang, D. Schnyer, D. Neikirk, N. Lu, "Cut-and-Paste" manufacture of multiparametric epidermal sensor systems. *Adv. Mater.* **27**, 6423–6430 (2015).

28. A. Gallina, T. Vieira, Territory and fiber orientation of vastus medialis motor units: A surface electromyography investigation. *Muscle Nerve* **52**, 1057–1065 (2015).

29. T. Yamamoto, Y. Yamamoto, Analysis for the change of skin impedance. *Med. Biol. Eng. Comput.* **15**, 219–227 (1977).

30. K. Nomizu, Kinematics and differential geometry of submanifolds. *Tohoku Math. J.* **30**, 623–637 (1978).

31. M. Raffaelli, J. Bohr, S. Markvorsen, in *Bridges 2016: Mathematics, Music, Art, Architecture, Education, Culture* (Tessellations Publishing, 2016), pp. 457–460.

32. O. S. Kim, in *2013 IEEE Antennas and Propagation Society International Symposium (APSURSI)* (IEEE, 2013), pp. 776–777.

33. L. Xiao, C. Zhu, W. Xiong, Y. Huang, Z. Yin, The conformal design of an island-bridge structure on a non-developable surface for stretchable electronics. *Micromachines (Basel)* **9**, 392 (2018).

34. S. Kabiri Ameri, R. Ho, H. Jang, L. Tao, Y. Wang, L. Wang, D. M. Schnyer, D. Akinwande, N. Lu, Graphene electronic tattoo sensors. *ACS Nano* **11**, 7634–7641 (2017).

35. W.-H. Yeo, Y.-S. Kim, J. Lee, A. Ameen, L. Shi, M. Li, S. Wang, R. Ma, S. H. Jin, Z. Kang, Y. Huang, J. A. Rogers, Multifunctional epidermal electronics printed directly onto the skin. **25**, 2773–2778 (2013).

36. E. R. Nadel, J. W. Mitchell, J. A. J. Stolwijk, Differential thermal sensitivity in the human skin. *Pflugers Arch.* **340**, 71–76 (1973).

37. I. Darian-Smith, K. O. Johnson, Thermal sensibility and thermoreceptors. *J. Invest. Dermatol.* **69**, 146–153 (1977).

38. D. Salter, in *Skin Bioengineering* (Karger Publishers, 1998), vol. 26, pp. 38–47.

39. K. Sato, in *Reviews of Physiology, Biochemistry and Pharmacology*, R. H. Adrian, E. Helmreich, H. Holzer, R. Jung, K. Kramer, O. Krayer, R. J. Linden, F. Lynen, P. A. Miescher, J. Piiper, H. Rasmussen, A. E. Renold, U. Trendelenburg, K. Ullrich, W. Vogt, A. Weber, Eds. (Springer Berlin Heidelberg, 1977), vol. 79, pp. 51–131.

40. M. A. Lopez-Gordo, D. Sanchez-Morillo, F. P. Valle, Dry EEG electrodes. *Sensors* **14**, 12847–12870 (2014).

41. J.-S. Blouin, G. P. Siegmund, M. G. Carpenter, J. T. Inglis, Neural control of superficial and deep neck muscles in humans. *J. Neurophysiol.* **98**, 920–928 (2007).

42. C. E. Stepp, J. T. Heaton, R. G. Rolland, R. E. Hillman, Neck and face surface electromyography for prosthetic voice control after total laryngectomy. *IEEE Trans. Neural Syst. Rehabil. Eng.* **17**, 146–155 (2009).

43. C. M. Sommerich, S. M. Joines, V. Hermans, S. D. Moon, Use of surface electromyography to estimate neck muscle activity. *J. Electromyogr. Kinesiol.* **10**, 377–398 (2000).

44. N. Rudigkeit, M. Gebhard, AMiCUS—A head motion-based interface for control of an assistive robot. *Sensors* **19**, 2836 (2019).

45. T. Widlund, S. Yang, Y.-Y. Hsu, N. Lu, Stretchability and compliance of freestanding serpentine-shaped ribbons. *Int. J. Solids Struct.* **51**, 4026–4037 (2014).

46. P. Chappuis, P. Pittet, E. Jéquier, Heat storage regulation in exercise during thermal transients. *J. Appl. Physiol.* **40**, 384–392 (1976).